Experimental Gravity with PSR B1534+12

by

Emmanuel Fonseca

B.Sc., The Pennsylvania State University, 2010

A THESIS SUBMITTED IN PARTIAL FULFILLMENT OF
THE REQUIREMENTS FOR THE DEGREE OF

MASTER OF SCIENCE

in

The Faculty of Graduate Studies

(Astronomy)

THE UNIVERSITY OF BRITISH COLUMBIA

(Vancouver)

October 2012

© Emmanuel Fonseca 2012

Abstract

We present an updated analysis of pulse profiles and their arrival-times from PSR B1534+12, a 37.9-ms pulsar that is orbiting a neutron star. Such "double-neutron-star" systems are expected to undergo various relativistic effects, such as orbital decay and precession, due to the strong-field nature of the local gravitational field (Damour & Taylor, 1992). A high-precision timing model is derived that accounts for all astrophysical processes that systematically affect pulse arrival-times. In the process of generating this model, we constrain parameters that characterize the interstellar environment, relative motion of the pulsar, its spin properties, and binary parameters. We measure five "post-Keplerian" parameters that represent relativistic corrections to the standard Keplerian quantities that describe a binary orbit. These relativistic parameters are then used to test general relativity by comparing the measured values with those predicted by Einstein's gravitational theory. We conclude that general relativity is confirmed to within $\sim 0.35\%$ of its predictions. The measurement of orbital decay contains a bias due to relative acceleration in the Galactic potential, and cannot be corrected for at this time due to an unreliable measure of distance; however, we can use this bias as a means to constrain the distance the pulsar should be from Earth in order for general relativity to be the correct theory of gravity. We find this distance to be $d_{\rm GR} = 1.037 \pm 0.012$ kpc. We also present evidence for pulse "jitter" in PSR B1534+12, which indicates short-term magnetospheric activity and has significant implications for the long-term improvement of timing precision. In a separate study, we present an analysis on pulse-profile evolution that has been previously linked to relativistic spin precession (Stairs et al., 2004). The current results of our precession analysis cannot confirm general relativity using this relativistic effect, but future studies and observations are needed constrain the precession rate of PSR B1534+12.

Preface

Several parts of our data set were acquired and used in previous studies of PSR B1534+12:

- The "Mark III data set" consists of pulse arrival-times and profiles that were recorded at Arecibo Observatory with the Mark III observing system, with a central observing frequency of 1400 MHz . This set was collected and prepared by Z. Arzoumanian, A. Wolszczan, and J. H. Taylor. Results obtained with this data set were published by Arzoumanian (1995) and Stairs et al. (1998), and a more recent analysis of this set was performed by Stairs et al. (2002).

- The "Mark IV data set" consists of pulse arrival-times and profiles that were recorded at the Arecibo Observatory with the Mark IV observing system, with central observing frequencies of 430 MHz and 1400 MHz. The set was collected and prepared by I. H. Stairs, S.E. Thorsett, J. H. Taylor, and A. Wolszszcan. Further observational support was given by K. Xilouris, D. Lorimer, D. Nice, E. Splaver, A. Lommen, P. Freire, and I. Hoffman. Results obtained with Arecibo Mark IV data taken up to early 2002 were published by Stairs et al. (2002). Several additional years of Mark IV data (up to late 2004) were presented in a preliminary version of the timing analysis described in this thesis (Stairs, 2005).

The global pulsar-timing and profile-evolution analyses presented below were carried out entirely by E. Fonseca. Moreover, this manuscript was written by E. Fonseca with invaluable commentary and feedback from I. H. Stairs and B. Gladman.

Table of Contents

Abstract ii

Preface iii

Table of Contents iv

List of Tables vi

List of Figures vii

Acknowledgements viii

Dedication ix

1 Introduction 1
- 1.1 Cosmic Lighthouses 2
- 1.2 Overview of Pulsar Timing 2
  - 1.2.1 Basic timing model 3
- 1.3 Pulsars in Binary Systems 5
  - 1.3.1 System evolution and double-neutron-star binaries . . 6
- 1.4 Pulsars and General Relativity 7

2 High-Precision Pulsar Timing of PSR B1534+12 9
- 2.1 A Brief History 9
- 2.2 Data Acquisition and Reduction 10
  - 2.2.1 Observing Machines 12
  - 2.2.2 Data Processing and Determination of TOAs 13
  - 2.2.3 Data Weights and Pulse Jitter in PSR B1534+12 . . 15
- 2.3 The timing model 15
  - 2.3.1 Solar-system corrections and astrometric parameters 17
  - 2.3.2 DM Variation over Time 18
  - 2.3.3 Theory-Independent Binary Model 22
  - 2.3.4 Fitting Procedure 24

2.4 Results and Interpretation 26
2.4.1 Tests of General Relativity 26
2.4.2 A Theoretical Distance Estimate to PSR B1534+12 . 29
2.4.3 Pulsar Jitter and Instrumental Limits on Timing Precision 33

3 Profile Evolution and Relativistic Spin Precession in PSR B1534+12 35
3.1 Data Reduction and Observing Strategy 38
3.2 Methodology 40
3.3 Current Results 43

4 Summary, Conclusions, and the Future 47

Bibliography 50

List of Tables

2.1 Data Logistics of Observing Machines 11
2.2 Fitted Astrometric, Spin, and DM parameters 19
2.3 Fitted orbital elements for PSR B1534+12 23

3.1 Pulse-profile logistics 37

List of Figures

1.1 Example of average profiles 4

2.1 ASP standard templates 14
2.2 Pulse jitter in PSR B1534+12. 16
2.3 DM variation with time. 21
2.4 Postfit residuals for PSR B1534+12. 25
2.5 Mass-mass plot. 28
2.6 Monte-Carlo sampling of Galactic, timing parameters 31
2.7 Distribution of theoretical distances to PSR B1534+12 32

3.1 PCA output for Mark IV and ASP profiles 39
3.2 Comparison of profile shapes 42
3.3 Mark IV precession results 45
3.4 ASP precession results 46

Acknowledgements

First and foremost, I would like to thank my supervisor, Ingrid Stairs, for her unwavering guidance and support. It has been a sincere pleasure to work with you over the last two years in the exciting field of pulsar astrophysics. This work would certainly not have been possible without your expertise, insight, and patience.

I would also like to thank members of the pulsar group here at the University of British Columbia (UBC), past and present, for making this graduate experience at UBC even more enjoyable and enlightening.

Many thanks are given to the astronomy faculty at UBC, as well as its Department of Physics and Astronomy, for accepting me into such a vibrant academic environment.

I would not be at UBC today without the supervision and support from: Stephen Holland; Scott Koch; Erik Hoversten; Peter Roming; and other members of the Swift Gamma-Ray Burst Mission at Penn State University. I thank you immensely for providing me with my first research opportunities in astronomy, as well as an informed sense of direction in my career.

I would like to thank Donald Schneider, for teaching one of the most challenging and memorable courses I have ever taken. Even during a period of immense doubt, you inspired me to learn more about how the Universe works, and provided me with the confidence to pursue graduate study.

Last and (certainly) not least, I would like to thank my parents, siblings, and friends for their love and constant support. Thank you for *everything*.

For my family,
my friends,
the Zen House,
and Paul Famiglietti.

Chapter 1

Introduction

The discovery of pulsars (Hewish et al., 1968) marked the beginning of a productive and insightful era in high-precision pulsar astronomy. Indeed, these rapidly-rotating, compact objects are among the most versatile tools in modern physics and astrophysics, lending themselves to a wide variety of studies and applications. For instance, the first confirmed extra-solar planets were discovered orbiting a millisecond pulsar (Wolszczan & Frail, 1992). Pulsars have also been used to estimate the distribution of free electrons in the Galaxy, which can then be used to infer distances to these objects from dispersive delays in multi-frequency pulsar signals (e.g. Taylor & Cordes, 1993). In a more recent application, high-precision mass estimates of pulsars in binary orbits have been used to constrain the equation of state of condensed stars (Demorest et al., 2010), as well as provide constraints on possible mass-transfer histories and subsequent evolutionary scenarios of massive binary systems (e.g. Stairs, 2004).

Pulsars are particularly powerful laboratories for measuring relativistic effects and testing alternate theories of gravitation. The discovery of PSR B1913+16, commonly known as the "Hulse-Taylor" pulsar (Hulse & Taylor, 1975), provided the first case where such an object in a strong gravitational field could be used to place substantial constraints on relativistic gravity. A significant measurement of orbital decay in the Hulse-Taylor binary system inferred the existence of gravitational radiation, a previously unconfirmed prediction of general relativity at that time (Taylor & Weisberg, 1982). Several other tests have since been performed using pulsars in different astrophysical environments, examining possible violations in relativistic equivalence principles and precession of pulsars about their spin axes; see Stairs (2003) for a review.

This thesis describes several analyses of PSR B1534+12, a pulsar in a binary orbit with another neutron star, and the implications these studies have on gravitational theory. In order to provide clarity and context for the details of this work, this chapter provides a comprehensive introduction and overview of the pulsar model used, as well as the modern techniques for studying pulsars that are applied to the studies outlined in the following

chapters. A review of pulsars in binary systems and tests of general relativity is also provided below.

1.1 Cosmic Lighthouses

A typical pulsar model is comprised of a rotating neutron star, formed from a supernova explosion, that emits beamed electromagnetic radiation at both magnetic poles. The magnetic axis is misaligned with the star's rotation axis and occasionally points in the direction of Earth, leading an observer to see "pulsed" emission. The compact object is highly magnetized, with a typical surface magnetic-field strength of $\sim 10^{10}$ Gauss, and is surrounded by a dense magnetosphere of charged particles that rotates with the star (Goldreich & Julian, 1969). Moreover, this dipolar misalignment induces electromagnetic waves that radiate away from the magnetosphere and result in a loss of rotational energy, or "spin-down", of the pulsar. Spin-down rates for "normal" (i.e. isolated) pulsars are typically $\sim 10^{-15}$ s/s, whereas binary and millisecond pulsars can have rates as low as $\sim 10^{-20}$ s/s; this discrepancy is believed to indicate past interaction between the pulsar and a binary companion (Lorimer & Kramer, 2005).

All neutron-star models describe a spherical, stellar object whose mass is contained within a characteristic radius of ~ 10 km. These objects are among the densest objects in the universe. Models of neutron-star structure indicate that pulsar masses can range between 0.1 and $\sim 3\ M_{\odot}$, although the upper limit is less certain due to complications from a general-relativistic treatment of the neutron-star equation of state (Lattimer & Prakash, 2004). A typical, theoretical structure of neutron stars depicts a thin outer crust and superfluid interior, with the star's matter density varying by six orders of magnitude from the star's surface to its center (Lyne & Smith, 2004). High-precision mass estimates of the most massive pulsars continue to provide sizable constraints on possible equations of state that govern the structure of such compact objects.

1.2 Overview of Pulsar Timing

Pulsars are often renowned for their rapid and stable rotation, which is reflected in the radio-pulse period. However, the key property of radio pulsars is the long-term stability of the pulse shape, or "profile", over time. Individual pulses are recorded as noisy profiles and vary dramatically in appearance. These irregularities vanish when one averages these individual

profiles together to form an average (or "integrated") pulse profile. See Figure 1.1 for a comparison of integrated profiles from PSR B1534+12 – the pulsar that is subject to this study – averaged over different time scales. The overall shape of the integrated profile remains remarkably stable and becomes sharper as more individual profiles are folded together, which allows it to serve as a type of "standard template" for the purposes of determining pulse arrival-times. In fact, integrated pulse profiles are crucial for studying the deviations between a pulsar signal's time of arrival (or "TOA") and all subsequent TOAs; this type of analysis is commonly referred to as "pulsar timing".

1.2.1 Basic timing model

The goal of pulsar timing is to account for every rotation of the neutron star and, by extension, model every physical process that systematically affects each TOA. In practice, the construction of a "timing model" for a given pulsar incorporates important details of the object and its local environment, as well as the Earth's motion about the Sun and its own spin axis. Pulse TOAs are initially recorded at a local-observatory time t and are subjected to these various forms of timing bias. Such analyses are therefore carried out in a stepwise manner by initially transforming the arrival-times measured at the observatory to an inertial reference frame[1], and assuming that the pulsar is isolated and slowing down due to magnetic dipole radiation. This permits the pulse phase ϕ that is recorded at a transformed arrival-time τ to be modeled using a simple Taylor expansion (e.g. Lorimer & Kramer, 2005),

$$\phi = \phi_0 + \nu(\tau - \tau_0) + \frac{1}{2!}\dot{\nu}(\tau - \tau_0)^2 + \frac{1}{3!}\ddot{\nu}(\tau - \tau_0)^3 + ... \qquad (1.1)$$

where ν is the pulsar rotation frequency, dots denote time-derivatives, and ϕ_0 and τ_0 are a reference phase and time, respectively. Additional astrophysical processes will manifest themselves as systematic delays in pulse TOAs. Parameters that characterize these delays can be measured with high precision by incorporating their theoretical timing-delay models into the arrival-time transformation. Furthermore, non-physical effects can occur due to instrumental deficiencies and/or differences in instrumental specifications when using timing data recorded with different signal processors (Taylor & Weisberg, 1989). It is usually necessary for the timing model to include arbitrary timing offsets when using data taken with multiple observing machines.

[1] This is usually taken to be the Solar-system barycenter.

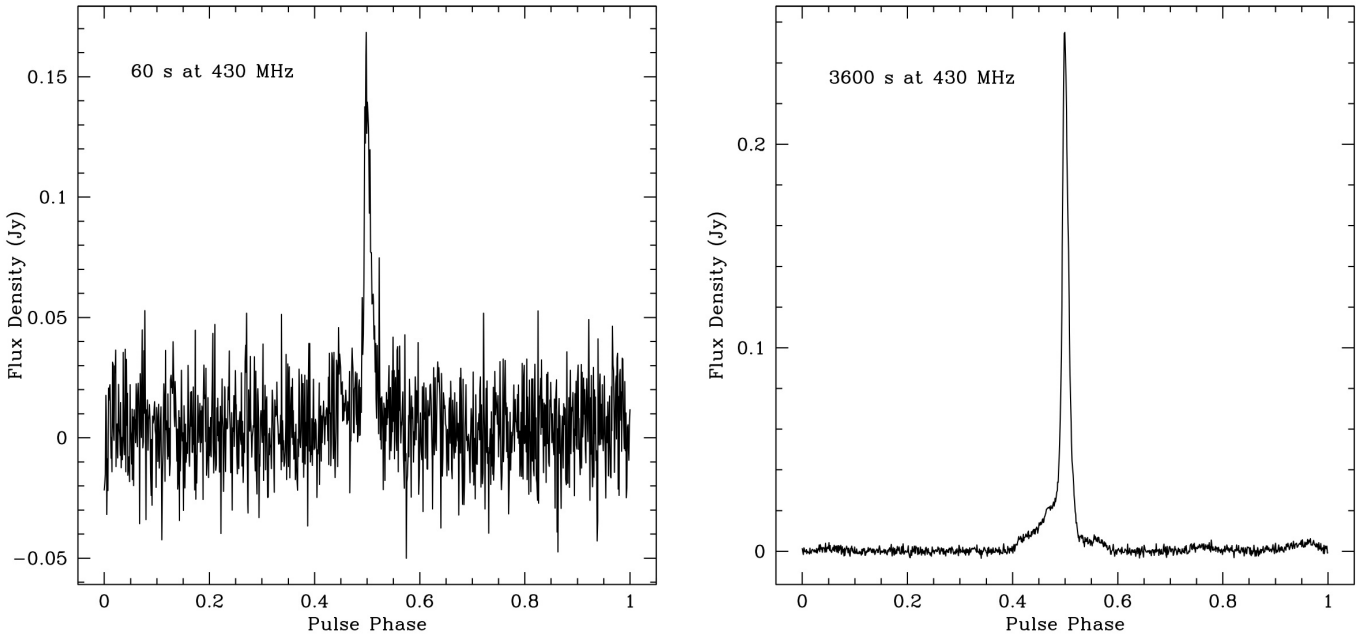

Figure 1.1: Two folded pulse profiles of PSR B1534+12 recorded with the Mark IV signal processor at the 305-m Arecibo Observatory. These two plots illustrate the long-term stability of pulse profiles, a property seen in nearly all radio pulsars.

1.3 Pulsars in Binary Systems

A pulsar undergoing binary motion with a massive object[2] will exhibit apparent changes in its rotation period and pulse TOA due to the Doppler effect. Such binary systems can be readily identified as periodic changes in the observed rotation period after transforming pulse TOAs to an inertial reference frame and fitting Equation 1.1 to the recorded (transformed) TOAs. Binary pulsars, with their spin and spin-down rates, can then be further characterized by the orbital elements of the binary system. This can be done by examining the variation of observed rotation period (P_{obs}) from its intrinsic value (P) over time due to Doppler motion:

$$P_{obs} = P\left(1 + \frac{V_1(A_e)}{c}\right) \tag{1.2}$$

where

$$V_1(A_e) = \frac{2\pi}{P_b}\frac{a\sin i}{\sqrt{1-e^2}}[\cos(\omega + A_e) + e\cos\omega] \tag{1.3}$$

is the projected, line-of-sight orbital velocity of the pulsar. The remaining parameters are further related to the orbital elements of interest through "Kepler's equations",

$$\omega = \omega_0 + \left(\frac{P_b\dot{\omega}}{2\pi}\right)A_e(u) \tag{1.4a}$$

$$A_e(u) = 2\arctan\left[\left(\frac{1+e}{1-e}\right)^{1/2}\tan\frac{u}{2}\right] \tag{1.4b}$$

$$u - e\sin u = 2\pi\left[\left(\frac{t-T_0}{P_b}\right) - \frac{\dot{P}_b}{2}\left(\frac{t-T_0}{P_b}\right)^2\right] \tag{1.4c}$$

where u is the "eccentric" anomaly, $A_e(u)$ is the corresponding "true" anomaly, and the remaining orbital parameters are summarized as follows: $x = a\sin i$ is the projected semi-major axis; e is the orbital eccentricity; P_b is the orbital period; ω is the longitude of periastron[3]; and T_0 is an epoch of periastron.

[2]Typical binary companions are other massive stars. However, several Earth-mass planets have been discovered through pulsar-timing studies (Wolszczan & Frail, 1992).

[3]In pulsar astronomy, ω is measured between the ascending node (the point where the pulsar crosses the plane of the sky and moves *away* from an observer) and the location of periastron.

Several quantities of interest – the pulsar mass (m_1), the companion mass (m_2), and inclination angle of the orbital plane relative to the plane of the sky (i) – usually cannot be measured directly through pulsar-timing studies. However, these parameters can be related to one another by the nominal mass function,

$$f_m = \frac{(m_2 \sin i)^3}{(m_1 + m_2)^2} = \frac{4\pi^2}{G} \frac{x^3}{P_b^2} \tag{1.5}$$

where the right-hand-side of Equation 1.5 can be readily computed. A minimum mass of the companion star can be approximated by assuming a typical pulsar mass of $m_1 = 1.35\ M_\odot$ and an edge-on orbital inclination ($i \approx 90°$).

Equations 1.2, 1.3, 1.4 can generally be used to obtain initial estimates of the orbital parameters, and adequately describe non-relativistic binary systems. In practice, high-precision measurements of orbital parameters are made by modeling the differences in pulse times-of-flight across the orbit as further systematic delays in pulse TOAs (Lorimer & Kramer, 2005). Furthermore, relativistic binary systems – where a pulsar orbits another compact object – will exhibit effects that are not accounted for in the above expressions. Additional models are needed to characterize the strong-field nature of such a system, and these are presented in Chapter 2 for the case of PSR B1534+12.

1.3.1 System evolution and double-neutron-star binaries

The combination of spin and orbital properties can also be used to infer the evolutionary history of the binary system (Lorimer, 2001). Many evolutionary scenarios involve the more-massive binary star evolving faster than its companion and eventually undergoing a supernova event, the remnant of which is a neutron star. Any bound, post-supernova binary system is therefore expected to become significantly more eccentric than its progenitor system due to the injection of post-explosion energy into the system. The most common of subsequent, interactive processes for these systems is the transfer of mass between stars, which can occur as the orbit shrinks in size. Moreover, a binary star will expand as it evolves during its sub-giant and giant phases of its lifetime. Both cases eventually lead the companion star to overflow the gravitational equipotential of the binary system, or "Roche lobe", where its mass is then streamed onto the compact object. This mass-accretion phase will result in an increase of angular momentum, or "spin-up", of the compact object, as well as damping of its magnetic-field strength and circularization of the orbit.

The end-products of these evolution schematics sensitively depend on several initial conditions, the more important of which are the masses of the two binary components (Stairs, 2004). A binary system with two very massive stars (each with a mass $m \geq 8\ M_{\odot}$) is thought to produce a neutron star and He star that is stripped of its main-sequence envelope after mass transfer; the He star will eventually explode and form another neutron star, finally leaving two neutron stars closely orbiting one another in an eccentric orbit. These kinds of systems are observationally rare, with only ten double-neutron-star binaries known (Lorimer, 2005). Nevertheless, these binary systems are near-ideal candidates for experimental gravity with high-precision pulsar timing.

1.4 Pulsars and General Relativity

Several modern tests of gravitational theory have been carried out within the Solar System and have confirmed general relativity with considerable precision (Everitt et al., 2011). However, these tests probe gravitation in a considerably "weak" gravitational field. A dimensionless parameter that quantifies gravitational-field strength at an object's surface is given by Damour & Taylor (1992) as

$$\alpha = \frac{GM}{c^2 R} \tag{1.6}$$

where G is Newton's constant, M is the mass of the object, c is the speed of light, and R is the radius of the object. The Sun has a strength value of $\alpha \sim 10^{-6}$ and is thus characterized as a "weak-field" object. In contrast, a neutron star has a typical value of $\alpha \approx 0.2$ and is subsequently considered a "strong-field" object. Pulsars therefore provide a significant and unique astrophysical laboratory for measuring relativistic effects in the strong-field regime of gravity, especially if they are in binary systems with other compact objects (Damour & Deruelle, 1985, 1986).

These strong-field effects are hereafter referred to as "post-Keplerian" (PK) parameters, which represent relativistic corrections to the standard Keplerian parameters defined in Section 1.3 above. The orbital decay of a relativistic binary system, which was first observed in the Hulse-Taylor binary system, is an example of such PK effects. In a given theory of gravity, these parameters will depend on a variety of orbital parameters. In the case of general relativity, the PK parameters can be expressed as functions of the binary-component masses which are not usually accessible through standard pulsar-timing procedures:

$$\mathrm{PK}_j = f_j(m_1, m_2) \tag{1.7}$$

where the left-hand-side of Equation 1.7 is the j^{th} PK parameter, and f_j is the corresponding equation for that parameter. The masses of the binary system can therefore be uniquely determined if two PK parameters are measured and expressions for these parameters are available within a given theory of gravity. Measurement of three PK parameters leads to an overdetermination of the system, meaning that the combination can be used to *test* the gravitational theory under consideration. The Hulse-Taylor pulsar provided the first test of general relativity in the strong-field regime, where orbital decay ($\dot{P}_b$), the time-rate of change of the periastron longitude ($\dot{\omega}$), and time-average gravitational redshift parameter (γ) were measured with significance (Taylor & Weisberg, 1982, 1989).

Chapter 2

High-Precision Pulsar Timing of PSR B1534+12

2.1 A Brief History

PSR B1534+12[4], a bright 37.9-ms pulsar, was discovered in 1990 and immediately noted to undergo binary motion with another object of stellar mass (Wolszczan, 1991). The companion star is believed to be another neutron star, based on the observed facts that: the size of the orbit is small ($\sim 1R_{\odot}$); there is no eclipsing event shown in the pulsar's residuals, despite a highly-inclined orbit with $i \approx 74^{\circ}$; and the measured spin-down rate of PSR B1534+12 is consistent with a model of an old pulsar having undergone an accretion process with its massive companion, resulting in a spun-up pulsar and another compact object orbiting one another (e.g. Stairs, 2004). As noted in the previous chapter, such binary systems can serve as critical laboratories for testing gravitational physics in the strong-field regime of gravity.

Indeed, a follow-up timing analysis of PSR B1534+12 demonstrated that the system was undergoing orbital decay at a measured rate that is in accordance with the predictions of general relativity (Stairs et al., 1998). Moreover, this analysis provided the first instance where up to five PK parameters were measured with favorable precision: the familiar $\dot{\omega} - \dot{P}_b - \gamma$ parameters, as well as the r and s parameters that characterize the Shapiro time-delay (Shapiro, 1964; Damour & Taylor, 1992). Thus, unlike the Hulse-Taylor pulsar, *several* tests of gravitational theory can be extracted from high-precision timing measurements of PSR B1534+12. Moreover, this pulsar provided the first case where a "non-mixed" test of relativity theory was obtained by only considering PK parameters that characterize the quasi-static (i.e. non-radiative) nature of the relativistic binary system (Taylor et al., 1992).

[4] "PSR" stands for "pulsating source of radio", the "B" indicates the B1950 coordinate-reference epoch, and the 1534+12 indicates the right ascension + declination of the object.

A more recent timing analysis of this pulsar, published in 2002, presented extensive measurements of astrometric, spin, and environmental parameters of the pulsar, as well as Keplerian and PK elements of the binary system (Stairs et al., 2002); the latter were used to confirm general relativity and obtain estimates of the pulsar and companion masses with favorable precision.

This chapter presents an updated, high-precision timing analysis of PSR B1534+12, using a data set that spans over twenty-two years in time. A description of the data acquisition and reduction, implementation of several timing models, and estimation of the ionized interstellar medium and its behavior across the time series is provided below. The results and their interpretation are presented in the last section.

2.2 Data Acquisition and Reduction

All data utilized in this analysis were obtained with the 305-m Arecibo radio telescope in Puerto Rico, using several generations of pulsar signal processors. Observations with Arecibo began as early as August 1990, and occurred as recently as February 2012. Data were recorded using two 430-MHz[5] receivers, as well as two 1400-MHz[6] ("L-band") observatory receivers. All observing systems described below collected data in the standard "timing" mode of pulsar observations: a series of recorded, consecutive pulses were folded modulo the apparent (or "topocentric") pulse period in order to generate raw, unweighted profiles measured at different polarization states. These polarization profiles are then weighted through flux calibrations, and then added to produce the total-intensity profiles used for the timing analysis.

[5] A line feed Carriage House 430-MHz receiver was used for observations carried out between MJD 48126-52965, 52967-53063, and on 53102. An upgraded, Gregorian Dome 430-MHz receiver was used for MJD 52966, 53064-53101, and 53103-55974. 430 MHz data acquired between MJD 48126-49430 were not used in this analysis, for reasons described in the text.

[6] A narrow-band, line feed 1400-MHz receiver was used between MJD 48178-49379. 1400-MHz data acquired from MJD 51022 up to January 2004 were obtained with a Gregorian Dome "L-narrow" receiver, and all other 1400-MHz data after this period were recorded using a Dome "L-wide" receiver.

Parameter	Mark III	Mark IV	Mark IV	ASP	ASP	ASP	ASP	ASP
Frequency (MHz) ..	1400	430	1400	424	428	432	436	1400
Bandwidth (MHz) .	40	5	5	64	64	64	64	64
Spectral Channels..	32	1*	1**	1	1	1	1	16***
Number of TOAs ..	1185	3102	664	1438	1444	1474	1468	312
Dedispersion type .	Incoh.	Coh.	Coh.	Coh.	Coh.	Coh.	Coh.	Coh.
Integration time (s)	300	190	190	180	180	180	180	180
Date span (years) .	1990-94	1998-2005	1998-2005	2004-12	2004-12	2004-12	2004-12	2004-12
RMS residual, σ_{rms}	6.44	4.75	7.15	4.91	4.86	5.20	5.54	8.56

Table 2.1: Logistics of data sets used in this pulsar-timing analysis of PSR B1534+12. All data were collected using the Arecibo Observatory. * Four sub-bands centered at 430 MHz were taken when the Mark IV data were originally recorded, but were averaged together to build signal strength. ** Two sub-bands centered at 1400 MHz were taken when the Mark IV data were originally recorded, but were also averaged together to build signal strength. *** The number of actual channels recorded sometimes varied due to computational limitations, so this value represents a typical number of channels used.

2.2.1 Observing Machines

A portion of the data used for this thesis were recorded with the Mark III (Stinebring et al., 1992) and Mark IV (Stairs et al., 2000a) pulsar observing systems. The Mark III system employed a "brute-force" approach of pulse de-dispersion[7] by separating the receiver's bandpass into distinct spectral channels using a filter bank, detecting the signal within each channel, and shifting the pulse profile by the theoretical amount of dispersive delay for alignment and coherent averaging. As an upgrade from this system, the Mark IV machine employed the now-standard coherent de-dispersion technique (Hankins & Rickett, 1975) that samples and filters the data stream *prior* to detection of the radio pulse. A series of digital filters applied in the frequency domain completely remove the predicted dispersion signatures while retaining even greater precision than the Mark III counterpart. See Stairs et al. (1998, 2002) for more details on these observing systems and reduction of data obtained with these machines.

The majority of data used in this study were obtained with the Arecibo Signal Processor (ASP), a further upgrade from the Mark III/IV systems (Demorest, 2007). The ASP retains the coherent de-dispersion technique for shifting pulse profiles to a common phase, but first decomposes the signals across a bandwidth of 64 MHz into a number of 4-MHz spectral channels that depends on the observing frequency. We used data collected with the four inner-most spectral channels centered on 430 MHz, and typically sixteen channels centered on 1400 MHz, due to limits in computer processing and the limited receiver bandpass. This decomposition is carried out with even greater data sampling than its Mark IV predecessor: the Mark IV machine used 4-bit data sampling in 5-MHz-bandpass observing mode and 2-bit sampling in 10-MHz-bandpass observing mode, whereas ASP always used 8-bit sampling. The coherent de-dispersion filter is then applied to the raw, channelized data, which is then folded modulo the topocentric pulse period within each channel and recorded to disk. Table 2.1 presents technical information on the TOAs acquired with these three observing systems.

It is important to note that there is a slight overlap in pulse TOAs between the Mark IV and ASP data sets. This overlap occurs between MJD 53358 and 53601. Despite this overlap in data, we incorporated TOAs acquired from both machines during this era due to the substantially larger ASP bandwidth and argued that this bandwidth difference does not produce many redundant data points.

[7]The effects of a tenuous, ionized interstellar medium on pulsar signals are discussed in Section 2.2.2.

2.2.2 Data Processing and Determination of TOAs

We used an in-house suite of programs and subroutines that embody the reduction methodology developed by Ferdman (2008) for further reduction of our raw, uncalibrated data. This collection of algorithms automate the statistical excision of radio-frequency interference, as well as the application of appropriate flux and polarization calibrations in order to obtain the true shape and intensity of pulse profile. A bright, unpolarized quasar[8] was observed at nearly every epoch in order to obtain data for flux calibration; comparison with the signal strength on and off the quasar and the signal strength of a noise diode pulsed at 25 MHz yielded the proper conversion from machine counts to pulse flux density.

We employed the standard procedure for calculating TOAs and observed pulse phases from our processed data. This involves the cross-correlation – in the frequency domain – between an integrated pulse profile and a standard template determined from initial observations (Taylor, 1992). This template-matching method assumes that the folded profile $P(t)$ is essentially equivalent to the standard template $S(t)$, where both P and S are defined over one whole pulse period; the most general expression that links the two is then given by

$$P(t) = a + bS(t - \phi_{obs}) + c(t) \tag{2.1}$$

where a characterizes a shift in baseline, b a change in amplitude, ϕ_{obs} a shift in pulse phase, and $c(t)$ characterizes noise across the pulse phase. A least-squares fitting procedure is used to determine ϕ_{obs} and its uncertainty for every integrated profile used in the analysis described in the following sections. The TOA for a given integrated profile is then determined by adding the phase shift ϕ_{obs} to its time-stamp near the middle of the integration.

The noise parameter c is minimized when using folded profiles, permitting a stronger determination of ϕ_{obs} and its corresponding TOA. As such, we employ an integration-time scheme that is outlined in Table 2.1. A standard template was derived for the Mark III and IV pulsar backends, and at each of the two frequencies. ASP 430-MHz TOAs were derived using the Mark IV standard templates shown in Figure 2.1 for each of the four innermost frequency channels centered at 430 MHz. TOAs derived from ASP 1400-MHz data were generated by collapsing all channelized data into one set of pulse profiles, in order to increase signal strength.

[8]The Arecibo Observatory list this quasar with (B1950) coordinates $\alpha = 14^{\rm h}42^{\rm s}, \delta = 10^{\circ}1'$.

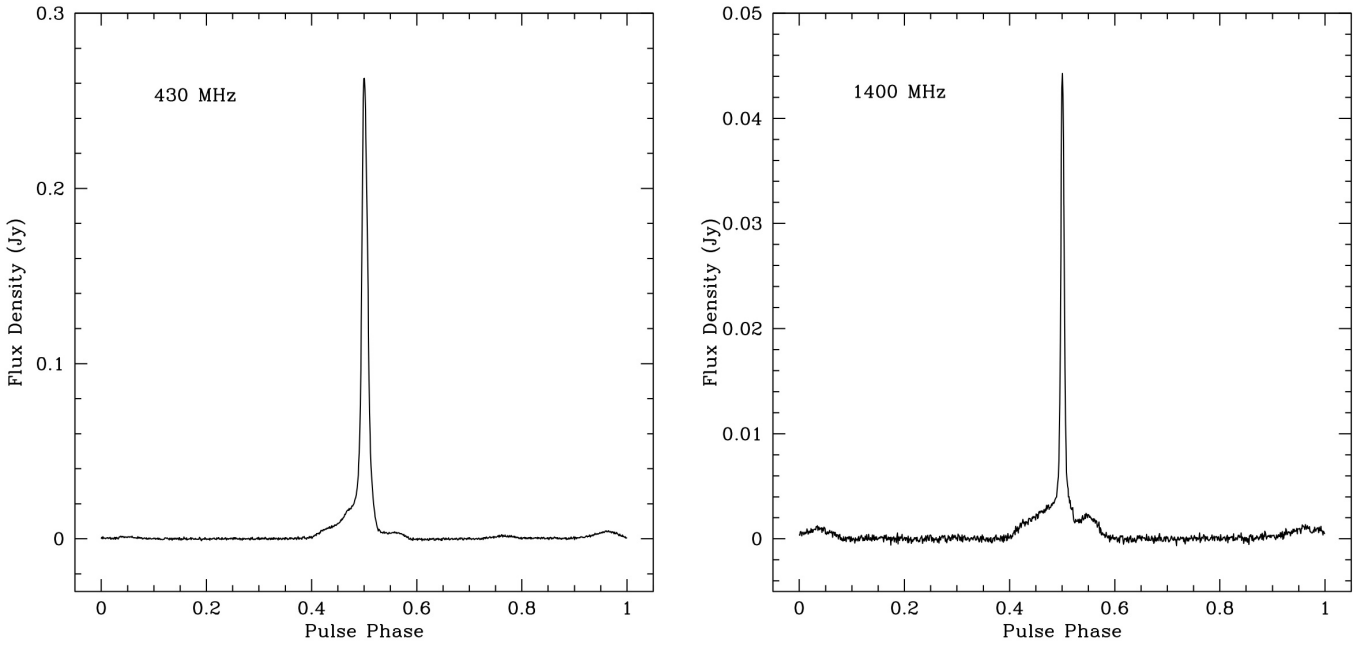

Figure 2.1: Standard templates used for determining ASP TOAs. These were derived by I. H. Stairs from data acquired with the Mark IV observing system, and were the same standard templates used in the Stairs et al. (1998, 2002) studies.

2.2.3 Data Weights and Pulse Jitter in PSR B1534+12

Taylor & Weisberg (1989) noted that uncertainties in TOAs determined by the least-squares fitting procedure described above only characterize random scatter in their estimation. Differences in instrumental specifications, whether with observatory receivers or signal processors, will introduce systematic errors that need to be allowed for or removed. We therefore assign a minimum error to each TOA data set by computing the goodness-of-fit χ^2 statistic for each set taken with the same receiver at the same frequency using a fixed timing solution. The amount of minimum error is then adjusted until $\chi^2/n \sim 1.0$, where n is the number of free parameters in the model, for all TOA data sets used.

We believe that the minimum-error strategy is justified since it allows us to retain the random contributions of TOA uncertainty (to some extent) while addressing possible sources of systematic error. While differences in instrumental properties are often the source for such uncertainties, another probable source of systematic error is illustrated in Figure 2.2. Post-fit residuals of unweighted PSR B1534+12 data obtained on MJD 53545 are plotted against orbital phase, where there is an overlap in timing data recorded by the Mark IV and ASP observing systems. The TOAs between machines unambiguously track each other across the orbit, despite substantial differences in instrumental specifications. We thus interpret this primarily as a reflection of physical instabilities, or "jitter" (Cordes & Shannon, 2012), in the magnetosphere of the pulsar. The jitter itself is a random process, but is essentially present across the entire data set and produces a spread in residuals about zero. The application of the minimum error per TOA allows this residual jitter to be accounted for while producing a timing solution that yields conservative estimates of parameter uncertainties.

2.3 The timing model

We used Equation 1.1 as our pulsar timing model for PSR B1534+12. However, it is important to note that the time τ in Equation 1.1 is a time of pulse emission in the rest frame of the pulsar, and not pulse TOAs that are initially measured at a telescope on Earth. Furthermore, many physical processes will affect every pulse and its corresponding TOA as it travels across the interstellar medium up until the moment of its detection. We therefore employ the time-coordinate transformation derived by Damour & Deruelle (1985, 1986) and used by Stairs et al. (1998, 2002) for PSR B1534+12,

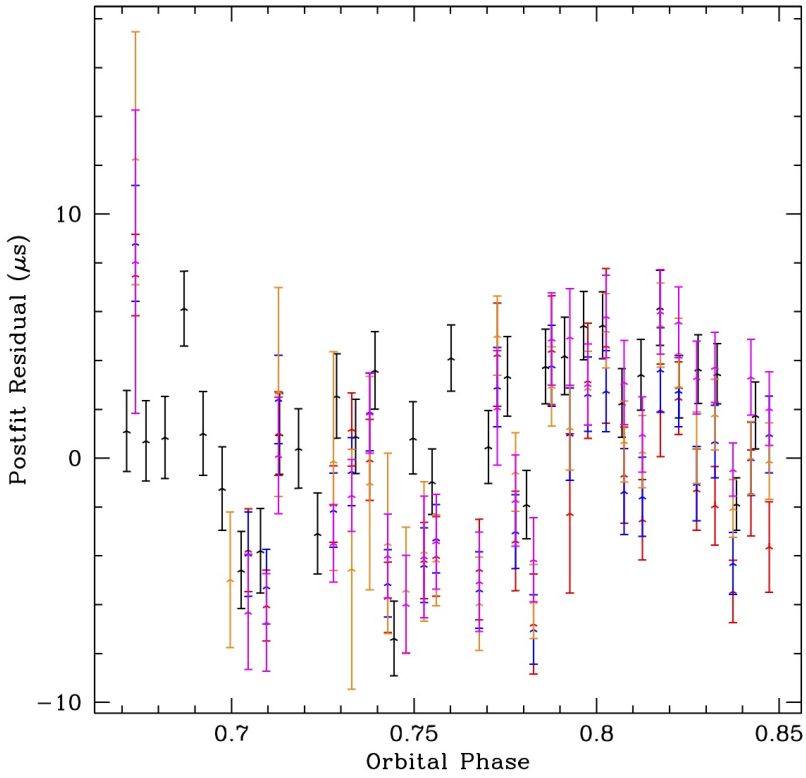

Figure 2.2: A plot of post-fit, pulse-phase residuals as a function of orbital phase for PSR B1534+12 at the epoch MJD 53545. Black points represent (unweighted) Mark IV 430 MHz data. Red, blue, orange, and magenta points represent (unweighted) ASP 424/428/432/436 MHz data, respectively. The Mark IV and ASP points generally track one another during the course of the orbit, despite substantial differences in technological specifications of the two observing systems. Moreover, all relevant processes are modeled in this unweighted fit. We therefore interpret this jitter as an indicator of short-term magnetospheric activity around the pulsar.

$$\tau = t - t_0 + \Delta_C - \Delta_{\rm DM} + \Delta_{R_\odot} + \Delta_{E_\odot} - \Delta_{S_\odot} - \Delta_R - \Delta_E - \Delta_S \quad (2.2)$$

to derive the barycentric arrival-time of pulse emission τ from the topocentric arrival-time t. The remaining terms and corrections are summarized as follows: t_0 is a reference epoch; Δ_C is the timing offset between the local (observatory) master clock and the reference standard of terrestrial time (taken as UTC(NIST)); $\Delta_{\rm DM}$ characterizes the time delay associated with frequency-dependent pulse dispersion due to intervening material; the $\Delta_\odot$terms represent the "Roemer", "Einstein", and "Shapiro" relativistic time delays in the Solar system; and the $\Delta_R, \Delta_E, \Delta_S$ terms are the analogous relativistic corrections for the pulsar binary system.

2.3.1 Solar-system corrections and astrometric parameters

The three solar-system timing delays in Equation 2.2 transform the arrival-times measured at the telescope to the inertial reference frame of the solar-system barycenter (SSB). Both the Shapiro and Einstein delays require careful consideration of local celestial bodies whose masses prominently affect the propagation of radio pulses by means of time dilation and gravitational redshift. These two delays are given by Lorimer & Kramer (2005) as

$$\Delta_{S\odot} = -2\sum_i \frac{GM_i}{c^3} \ln\left[\frac{\hat{s}\cdot\vec{r}_i^E + r_i^E}{\hat{s}\cdot\vec{r}_i^P + r_i^P}\right] \quad (2.3a)$$

$$\frac{d\Delta_{E\odot}}{dt} = \sum_i \frac{GM_i}{c^2 r_i^E} + \frac{v_E^2}{2c^2} - \text{constant} \quad (2.3b)$$

where M_i is the mass of the $i^{\rm th}$ body, $\vec{r}_i^E$ is the position vector of the telescope relative to the body, $\vec{r}_i^P$ is the position vector of the pulsar relative to the body, $\vec{v}_E$ is the velocity of the Earth at that instant, and $\hat{s}$ is a unit vector that points from the SSB to the pulsar. In practice, the Sun and the most massive planet - Jupiter - have measurable effects on pulsar timing (Backer & Hellings, 1986). Thus, we use the JPL DE414 planetary ephemeris (Konopliv et al., 2006) in this study, with its high-precision relative positions of these massive objects throughout the years, in order to properly transform our TOAs over the course of our data set to the SSB reference frame.

The position of PSR B1534+12 is measured through the annual variation of the Roemer timing delay, also given by Lorimer & Kramer (2005) as

$$\Delta_{R_\odot} = -\frac{1}{c}\left(\vec{r}_{SSB} + \vec{r}_{EO}\right) \cdot \hat{s} \tag{2.4}$$

where $\vec{r}_{SSB}$ is a position vector that points from the SSB to the center of the Earth, and $\vec{r}_{EO}$ is the position vector that points from the Earth's center to the telescope. The vector $\vec{r}_{SSB}$ as a function of time is given by the DE414 ephemeris, and the $r\vec{_{EO}}$ positions are provided through UT1 corrections of the Earth's non-uniform rotation, calculated by the International Earth Rotation and Reference Systems Service[9]. Moreover, rates of change in the position coordinates are measured through the relative motion between the binary system and the SSB. A timing parallax is also fitted for in the overall timing procedure.

2.3.2 DM Variation over Time

Radio pulses emitted simultaneously at different frequencies will be recorded at different arrival times on Earth. This delay arises from the frequency dependence of the pulse's group velocity as it traverses a tenuous interstellar medium. Therefore, pulsars with broadband radio emission will exhibit timing delays between TOAs measured at two different observing frequencies due to the dispersive nature of the electronic material along the line of sight. This offset between TOAs must be taken into account when applying the model in Equation 2.2 to multi-frequency data sets.

This timing delay $\Delta_{\rm DM}$ due to intervening material permits the calculation of a "dispersion measure" (DM),

$$\mathrm{DM} = \int_0^d n_e(l,t)dl \tag{2.5}$$

where d is the distance to the pulsar and $n_e(l,t)$ is the mean electron density along the line of sight l at a particular time t, by using the relation

$$\Delta_{\rm DM} = \frac{\mathrm{DM}}{2.41 \times 10^{-4} f^2} \tag{2.6}$$

where f is the observing frequency with units of MHz and the delay is in units of seconds (Manchester & Taylor, 1977). Observed values of DM range between $\sim 3{-}1500$ cm^{-3} pc[10]. This quantity is of particular interest because a distance to the pulsar can be inferred purely by its DM through Equation 2.5, given a model for the electron density along the path (Lyne et al., 1985;

[9] http://hpiers.obspm.fr

[10] http://www.atnf.csiro.au/people/pulsar/psrcat/

Parameter	Value
Right Ascension, α (J2000)	$15^{\rm h}37^{\rm m}09^{\rm s}.961716(6)$
Declination, δ (J2000)	$11^\circ55'55''.43372(14)$
Proper motion in R.A., μ_α (mas yr^{-1}) ..	1.494(15)
Proper motion in Decl., μ_δ (mas yr^{-1}) ..	-25.27(3)
Timing parallax, π (mas)	0.7(4)
Parameter reference epoch (MJD)	52077
Rotational frequency, ν (Hz)	26.3821327768945(2)
First frequency derivative, $\dot{\nu}$ (10^{-15} Hz^2)	-1.686089(4)
Second freq. derivative, $\ddot{\nu}$ (10^{-29} Hz^3) ..	9.8(1.7)
Third freq. derivative, $\dddot{\nu}$ (10^{-36} Hz^4) ...	-3.0(4)
Dispersion measure, DM 1 (cm^{-3} pc) ...	11.61944(2)*
DM derivative 1 (cm^{-3} pc yr^{-1})	-0.000316(10)*
Bin 1 range, epoch (MJD)	48126-50774, 48778*
DM 2 (cm^{-3} pc)	11.61631(3)
DM 2 derivative (cm^{-3} pc yr^{-1})	-0.000039(18)
Bin 2 range, epoch (MJD)	50775-52600, 51687.5
DM 3 (cm^{-3} pc)	11.61544(4)
DM 3 derivative (cm^{-3} pc yr^{-1})	-0.000298(14)
Bin 3 range, epoch (MJD)	52601-54300, 53450.5
DM 4 (cm^{-3} pc)	11.615712(6)
DM 4 derivative (cm^{-3} pc yr^{-1})	0.00085(4)
Bin 4 range, epoch (MJD)	54301-55125, 54713
DM 5 (cm^{-3} pc)	11.61641(14)
DM derivative 5 (cm^{-3} pc yr^{-1})	-0.00038(8)
Bin 5 range, epoch (MJD)	55126-56000, 55563

Table 2.2: Fitted astrometric, spin, and DM parameters for PSR B1534+12. Values in parentheses denote the uncertainty in the preceding digit(s).
* These values are taken from Stairs et al. (2002), but the date range is extended so that bins 1 and 2 are contiguous. See text for a brief discussion of this bin extension.

Taylor & Cordes, 1993; Cordes & Lazio, 2002). The time dependence of the electron density n_e is generally negligible when considering time series that span days or weeks.

Stairs et al. (1998, 2002) noted that a measurable change in DM of PSR B1534+12 could be extracted from their time series, which incorporated over ten years of timing data. They argued that, while the measured value of DM at a particular epoch is subject to biases in several forms (e.g. difference in standard profiles between the several signal processors), the DM *evolution* over time is real and reflects physical changes in the electron content along that direction. It is therefore important to account for these long-term changes in DM and remove the appropriate amount in the transformation given by Eq. (2.2) in order to obtain accurate estimates of parameters with the most favorable precision. An initial, ideal strategy for TOA de-dispersion was to fit for offsets of DM from a pre-defined value in small bin sizes of 80 days across the Mark IV and ASP data sets[11]. However, the numerous free parameters resulting from this strategy led to a lack of desirable precision, as well as noticeable covariances with several model parameters.

We ultimately decided to employ the same technique used by Stairs et al. (2002) of measuring DM in large bins and fitting for time-derivatives within each bin. Five DM bins are applied to our data set, with each bin reporting an average epoch, a DM at that epoch, and a first-derivative that characterizes linear change within the entire bin. A nominal value of DM can then be determined for any TOA within that bin through a straightforward linear calculation. Due to the exclusion of Mark III 430-MHz data, we used and fixed the values of the Mark III DM bin while allowing all other bins and their parameters to float. We also extended the original Mark III bin used in Stairs et al. (1998) so that it was contiguous with the first Mark IV bin; there are no timing data in this extension region, so increasing the bin size has no effect on DM measurements in this analysis. See Figure 2.3 for a graphical representation of DM evolution for PSR B1534+12, as well as Table 2.2 for values and their quoted uncertainties. The timescale and magnitude of DM evolution in PSR B1534+12 are comparable to changes seen in other pulsars in different directions (e.g. Kaspi et al., 1994; Ramachandran et al., 2006).

In principle, the solar wind can contribute to the dispersive delay of a radio pulse as it traverses the local Solar System, and the contribution

[11] The Mark III 430-MHz data set is excluded from this timing analysis due to systematic errors attributed to imperfections in pulse-dispersion removal prior to coherent folding of profiles (Stairs et al., 1998). However, it was still used by Stairs et al. (1998, 2002) to determine the evolution of DM across the Mark III data set; we use their result for the Mark-III DM parameters, while fitting for the other DM blocks.

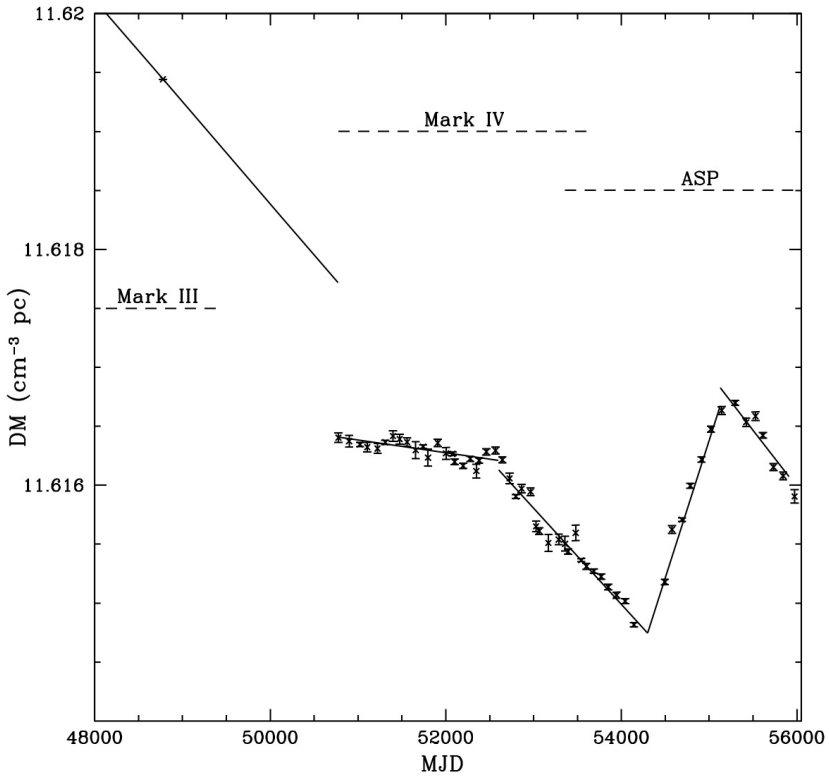

Figure 2.3: DM variation with time. Solid lines indicate linear change in DM across the bin, while dashed lines indicate the time span of data acquired with a labeled observing system. We extended the upper-bound of the Mark III bin from the last day of Mark III data acquired (MJD 49430) to the day before Mark IV data was first taken (MJD 50774) in order to make the bins contiguous; no data exists in this extension period, and so the extension of the bin does not affect DM measurements. The points and their error bars are estimated by fixing all newly-determined parameters, and fitting for DM in uniform block sizes of 80 days using the TEMPO pulsar timing software. The large DM bins were used to obtain global timing solution, and the data points were fitted separately to confirm that this choice in DM modeling was valid.

is dependent on the location of the observatory over the course of Earth's orbit about the Sun (You et al., 2007). This solar-DM component is most prominent for pulsars that lie close to the ecliptic plane. The position of PSR B1534+12 in Table 2.2 indicates that the object lies $\sim 30^\circ$ above the ecliptic plane. Moreover, the expected solar contribution to DM was calculated to be much lower than was seen in the actual scatter of the 80-day DM points in Figure 2.3. A further motivation for neglecting the solar-wind component was an unexpected covariance with the timing parallax; a non-zero solar component caused the inferred distance to be twice as small than the value expected from theoretical estimates (see section 2.4.2). We therefore chose to ignore the solar contribution to DM, while acknowledging that our timing parallax is likely not reliable as a fitted parameter.

2.3.3 Theory-Independent Binary Model

The orbital elements of interest are coded within the three relativistic time delays for the pulsar binary system, given by Damour & Deruelle (1986) as

$$\Delta_R = x \sin\omega(\cos u - e) + x(1-e^2)^{1/2}\cos\omega\sin u \tag{2.7a}$$

$$\Delta_E = \gamma \sin u \tag{2.7b}$$

$$\Delta_S = -2r \ln\big(1 - e\cos u - s[\sin\omega(\cos u - e) + (1-e^2)^{1/2}\cos\omega\sin u]\big) \tag{2.7c}$$

where the eccentric anomaly u is further related to the desired orbital parameters through Kepler's equations shown in Equations 1.4.

The Damour-Deruelle (DD) timing model we used to describe the delay in pulse propagation due to orbital motion incorporates up to 10 free parameters that are implicitly defined in Equations 1.4 and 2.7. These expressions were derived with minimal consideration to a particular theory of gravity, allowing for direct comparisons and tests of various frameworks that predict certain values for the relativistic corrections to the orbit (Damour & Taylor, 1992). Five of these parameters are the conventional Keplerian parameters: the orbital period P_b; the projected semi-major axis $x = a\sin i/c$; the orbital eccentricity e; and the longitude ω and epoch T_0 of periastron. The remaining five parameters are the PK effects that characterize the radiative and quasi-static nature of the relativistic binary system: the orbital decay $\dot{P}_b$; the advance of periastron $\dot{\omega}$; the time-dilation and gravitational-redshift parameter γ; and the range r and shape s of the Shapiro time delay.

Parameter	DD Model	DDGR Model
Projected semimajor axis, x (s)	3.7294637(12)	3.7294639(3)
Eccentricity, e	0.27367743(16)	0.27367734(8)
Epoch of periastron, T_0 (MJD)	52076.82711327(2)	52076.82711327(4)
Orbital Period, P_b (days)	0.420737298876(6)	0.420737298877(2)
Argument of periastron, ω (deg)	283.30601(3)	283.30602(2)
Rate of periastron advance, $\dot{\omega}$ (deg yr^{-1}) ...	1.755792(4)	1.7557927*
Time-averaged gravitational redshift, γ (ms)	2.072(1)	2.0709*
Orbital decay, $(\dot{P}_b)^{\rm obs}$ (10^{-12})	-0.1367(6)	-0.19244*
Shape of Shapiro delay, $s = \sin i$	0.978(3)	0.97469*
Range of Shapiro delay, $r = T_\odot m_2$ (μs)	6.5(6)	6.628*
Companion mass, m_2 ($M_\odot$)	1.3(1)	1.3458(4)
Pulsar mass, m_1 ($M_\odot$)	n/a	1.3326(4)*
Total mass, $M = m_1 + m_2$ ($M_\odot$)	n/a	2.678456(8)
Excess $\dot{P}_b$ (10^{-12})	n/a	0.0556(6)

Table 2.3: Experimental and theoretical values of orbital elements for PSR B1534+12. Note that the values in parentheses denote the uncertainty in the preceding digit(s).
* derived quantity

2.3.4 Fitting Procedure

In accordance with modern pulsar-timing techniques, the solution to the timing model given by Equations 1.1 and 2.2 is determined by minimizing the expression

$$\chi^2 = \sum_i \left(\frac{\phi(\tau_i) - \phi_{obs}(\tau_i)}{\sigma_i} \right)^2 \tag{2.8}$$

where τ_i is the transformation of the i^{th} TOA, $\phi(\tau_i)$ and $\phi_{obs}(\tau_i)$ are the corresponding expected and measured pulses phases, respectively, and σ_i is the uncertainty in the corresponding TOA. The uncertainties in fitted parameters are determined by the covariance matrices computed from the algorithms applied during the global fit for the timing solution.

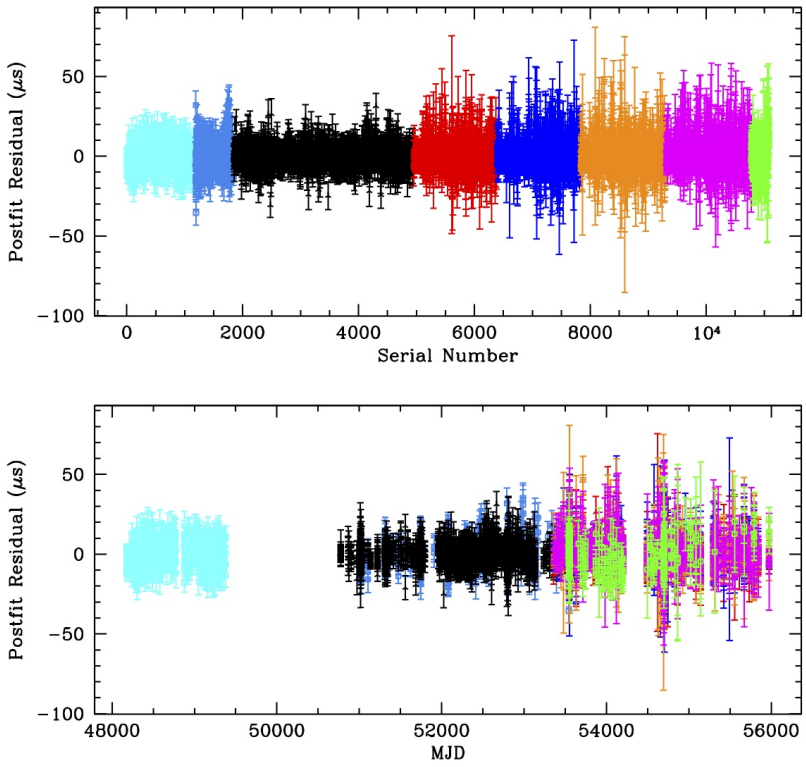

Figure 2.4: Postfit residuals for PSR B1534+12. Top panel indicates the data subsets by color, and the bottom plan plots residuals over the time span of our total set. Light-blue points represent Mark III 1400 MHz data; medium-blue and black points represent Mark IV 1400 MHz and 430 MHz data, respectively; red, blue, orange, magenta and green points represent ASP 424/428/432/436 MHz and 1400 MHz data, respectively. Later data (particularly the ASP 1400-MHz set) are more scattered due to smaller spectral channels at ASP 430 MHz, and a decreasing flux density over time at 1400 MHz. The global-fit reduced-$\chi^2 = 1.043$. The weighted root-mean-square residual is $\sigma_{rms} = 5.25$ μs.

2.4 Results and Interpretation

We used the TEMPO pulsar-timing software package[12], a comprehensive analysis tool that incorporates all of the aforementioned processes, ephemerides, and clock corrections when determining our timing model. TEMPO also provides various binary models that users can choose to include into their timing model; in our case, we chose the DD model as the binary description. Pulse-phase residuals for the global fit are displayed in Figure 2.4. The large amount of scatter seen in the ASP 1400-MHz data is due to a decreasing flux density at that observing frequency. Furthermore, the DM measurements during this era come almost entirely from the four ASP 430-MHz channels, so the (less numerous) ASP 1400-MHz points receive less weight in our fit, and are therefore slightly offset from zero. This offset likely reflects unmodeled frequency-dependent changes in the pulse profile.

Previous timing studies of PSR B1534+12 used the DE200 planetary ephemeris (Standish, 1990), the standard timing ephemeris during that era. We switched to the newer DE414 ephemeris and fitted our timing model so that the parameter values were extracted and reported with respect to a certain epoch, which we took as the midpoint of our data set. Therefore, direct comparison between parameter values presented in Tables 2.2, 2.3 and previously reported results will not be consistent. As a check, we carried out a global fit using the DE200 ephemeris and were able to reproduce the timing solution reported by Stairs et al. (2002). The key difference between solutions was the improved precision from our analysis, mainly due to a significantly extended data set that was collected from the upgraded ASP observing machine. All fitted-parameter errors reported by TEMPO are subsequently doubled, in accordance with previous timing analyses of this pulsar. This is strictly because our TOA uncertainties have effectively been increased when using the minimum-uncertainty approach mentioned above; this doubling is standard practice in pulsar timing when arrival-time uncertainties have been increased significantly. We therefore believe that uncertainties reported Tables 2.2, 2.3 reflect conservative estimates of the true 68%-confidence uncertainties.

2.4.1 Tests of General Relativity

A key advantage of the DD timing framework is that its derivation has minimal consideration to any particular theory of gravity (Damour & Deruelle,

[12] http://tempo.sourceforge.net

1985, 1986; Damour & Taylor, 1992). Therefore, the values of orbital elements presented in Table 2.3 can be directly compared to values predicted by any theory where expressions for the PK parameters are available. In the case of general relativity, the five PK parameters can be expressed in terms of the standard Keplerian parameters, the pulsar mass m_1, and the binary-companion mass m_2:

$$\dot{\omega} = 3\left(\frac{P_b}{2\pi}\right)^{-5/3}(T_\odot M)^{2/3}(1-e^2)^{-1}, \tag{2.9a}$$

$$\dot{P}_b = -\frac{192\pi}{5}\left(\frac{P_b}{2\pi}\right)^{-5/3}\left(1+\frac{73}{24}e^2+\frac{37}{96}e^4\right)(1-e^2)^{-7/2} \times T_\odot^{5/3} m_1 m_2 M^{-1/3}, \tag{2.9b}$$

$$\gamma = e\left(\frac{P_b}{2\pi}\right)^{1/3} T_\odot^{2/3} M^{-4/3} m_2(m_1+2m_2), \tag{2.9c}$$

$$r = T_\odot m_2, \tag{2.9d}$$

$$s = x\left(\frac{P_b}{2\pi}\right)^{-2/3} T_\odot^{-1/3} M^{2/3} m_2^{-1} = \sin i \tag{2.9e}$$

where $M = m_1 + m_2$ is the total mass of the binary system in solar units, and $T_\odot = GM_\odot/c^3 = 4.925490947\ \mu$s.

The two stellar masses are the only a priori unknowns, as the Keplerian and PK quantities are readily measurable to high precision through procedures outlined in the previous section. Moreover, the masses of the binary components can be uniquely derived if two PK parameters are measured with significance. Consistency checks can be performed if additional PK parameters are extracted, and these checks are physically interpreted as tests of the gravitational theory under consideration.

A standard representation of such tests is shown in Figure 2.5. Equations 2.9 are functions of the system masses, and all other parameters are fitted for in our DD-model timing solution. It follows that each equation can be inverted to put one mass as a function of the other. An $m_1 - m_2$ plane can then be defined, where each inverted equation represents a curve on such a plane (Taylor & Weisberg, 1989). For consistency in the strong-field regime, all curves must intersect at a common point. In practice, each curve has an upper and lower bound as dictated by the determined uncertainty in the measurement; all curves must therefore overlap a common area in this mass-mass space in order for the theory to be self-consistent. Figure 2.5 shows

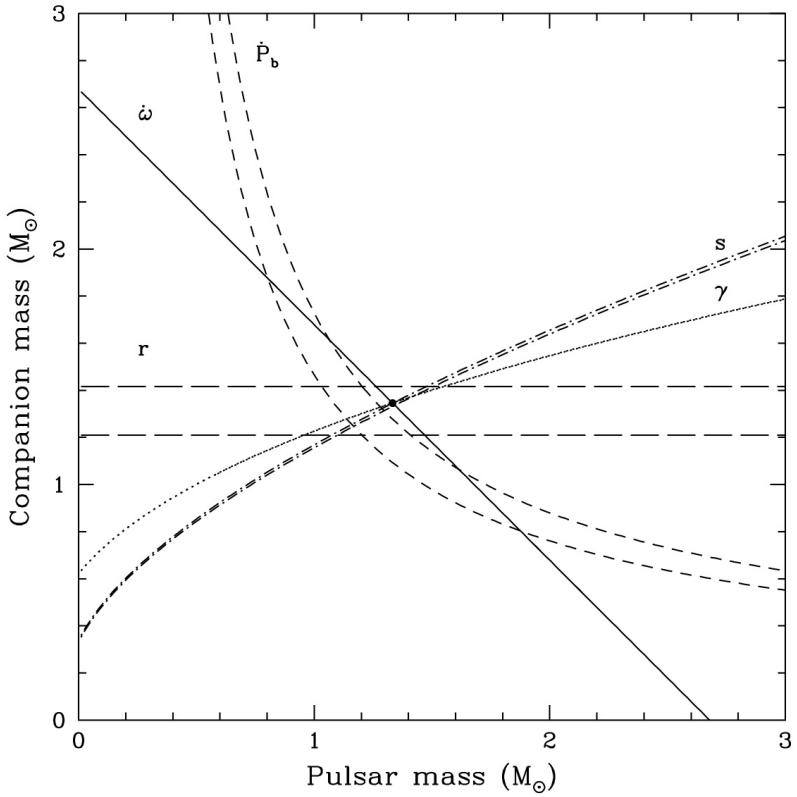

Figure 2.5: Mass-mass plot for PSR B1534+12. Nearly all five curves intersect at a common area on the space, producing two stringent tests of general relativity. The filled circle represents the theoretical (DDGR) masses of the two binary components: $[m_1, m_2]_{\rm DDGR} = [1.3458(4), 1.3326(4)]\ M_\odot$. The $\dot{P}_b$ curve is corrected for relative acceleration in the Galactic potential, which depends on an independent measure of distance. The uncertainty in this corrected curve is dominated by the uncertainty in the distance used. See the text for our interpretation of the non-agreement in the $\dot{P}_b$ measurement.

that four of the five curves intersect a common area, therefore producing two positive tests of general relativity[13].

The TEMPO software provides an additional relativistic binary model that assumes that general relativity is the correct theory of gravity. This "DDGR" binary model uses the DD-model values of the PK quantities as fixed parameters, as well as Equations 2.9, in order to determine the theoretical values of the two component masses. It also calculates the theoretical values of the PK parameters that are associated with the fitted masses, as well as an "excess" $\dot{P}_b$ to allow for the discrepancy between the expected and measured values of orbital decay. These values are reported in Table 2.3, and show strong agreement between experiment and theory within the quoted uncertainties.

In terms of precision, the $\dot{\omega}-\gamma-s$ combination provides the strongest test from the PSR B1534+12 system. The range in Shapiro delay is measured with significant but comparatively less favorable precision, and the measured rate of orbital decay is known to contain biases due to relative motion in the Galactic potential (see next section). A quality of this test can be inferred by considering the relative errors of the three $\dot{\omega} - \gamma - s$ parameters, which suggests that this test constrains general relativity to within ~ 0.35 % of its predictions. This crude estimate is nearly an order of magnitude larger than the tests performed on the double-pulsar system (Kramer et al., 2006), and so the test serves as a less stringent but still useful, independent check of gravitational theory. The derived mass estimates of PSR B1534+12 and its companion are among the most precise stellar masses measured to date, and rival those of the Hulse-Taylor system in precision (Weisberg et al., 2010). The significant difference in stellar mass between these two neutron stars advocates the possibility of mass inversion during the mass-transfer stage of binary evolution (Stairs et al., 2002).

2.4.2 A Theoretical Distance Estimate to PSR B1534+12

Equation 2.9b gives the value of $\dot{P}_b$ as measured in the reference frame of binary center-of-mass (Damour & Taylor, 1992). However, the observed value of $\dot{P}_b$ that we extracted from our time series is measured with respect to the SSB. Therefore, we corrected the observed value of $\dot{P}_b$ to the value measured in the binary center-of-mass reference frame via the transformation provided by Nice & Taylor (1995),

[13]The reason why $\dot{P}_b$ does *not* intersect the same area is explained in the next section.

$$\left(\frac{\dot{P}_b}{P_b}\right)^{\rm gal} = -\frac{a_z \sin b}{c} - \frac{v_0^2}{cR_0}\cos b\left(\cos l + \frac{\beta}{\sin^2 l + \beta^2}\right) + \mu^2\frac{d}{c} \qquad (2.10)$$

prior to applying the tests and generating Figure 2.5 discussed that are in the previous subsection. Here, a_z is the vertical component of Galactic acceleration as modeled by Kuijken & Gilmore (1989), $(b, l) = (0.8437181, 0.3464022)$ radians are the Galactic coordinates of PSR B1534+12, v_0 is the solar-system velocity about the Galactic center, R_0 is the distance of the Sun to the Galactic center, d is the distance to the pulsar, $\beta = (d/R_0)\cos b - \cos l$, and μ is the pulsar's proper motion. The last term in Equation 2.10 represents the "Shklovskii" correction (Shklovskii, 1970). An estimate of the pulsar distance was determined by assuming a model of the electron number density in the direction of the pulsar (Taylor & Cordes, 1993), as well as using the determined value of DM and Equation 2.5; using this model, $d = 0.7 \pm 0.2$ kpc. The pulsar coordinates and proper motion μ were determined through the pulsar timing techniques outlined above. The Galactic parameters were taken to be: $v_0 = 254 \pm 16$ km s^{-1}; $R_0 = 8.4 \pm 0.6$ kpc; and $a_z/c = (1.60 \pm 0.13) \times 10^{-19}$ s^{-1}. Values for the Galactic parameters were taken from Weisberg et al. (2010).

We then determined the "true" value of $\dot{P}_b$ by subtracting the Galactic contribution found in Equation 2.10 from the observed value reported in Table 2.3:

$$(\dot{P}_b)^{\rm true} = (\dot{P}_b)^{\rm obs} - (\dot{P}_b)^{\rm gal} \qquad (2.11)$$

Upper and lower bounds on $(\dot{P}_b)^{\rm true}$ are plotted in Figure 2.5. As is shown in the figure, the transformed value of $\dot{P}_b$ still cannot be brought into agreement with the other four PK quantities. We attributed this discrepancy to a deficiency in the electron-content model used to determine the pulsar distance by means of DM. A more recent electron number-density model was developed by Cordes & Lazio (2002), but cannot be used as it sets the theoretical distance to PSR B1534+12 calculated by Stairs et al. (2002) as a calibrating distance for their model. The bloated uncertainty in the transformed value is dominated by the rough DM-estimate of the pulsar's distance.

Bell & Bailes (1996) first noted that observed orbital-period derivatives could be used to determine precise distances to binary pulsars that are more reliable than distances from DM measurements or from timing parallaxes. For PSR B1534+12, this can be done by assuming that general relativity is

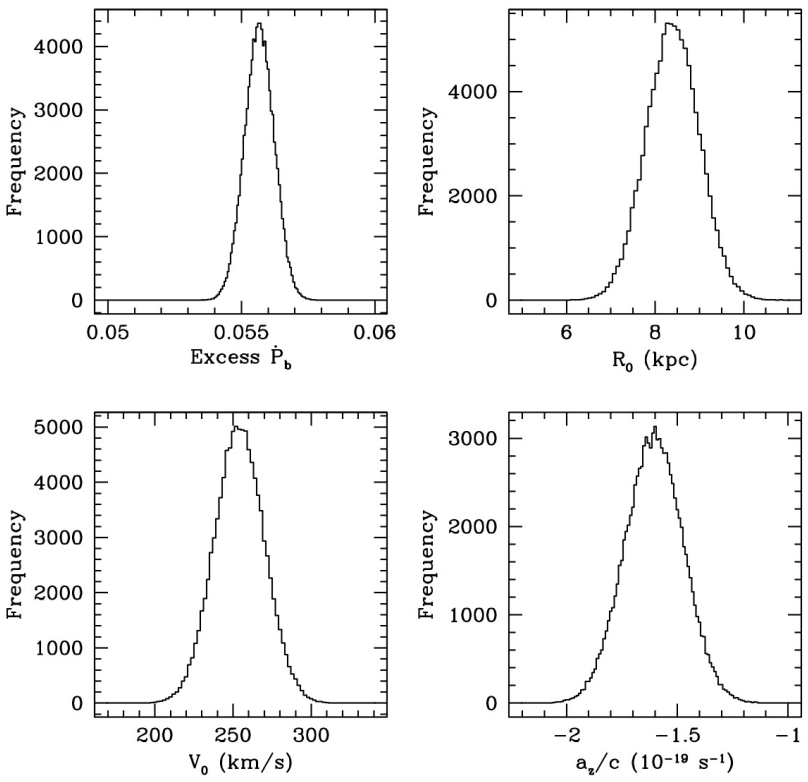

Figure 2.6: Monte-Carlo sampling of Galactic and pulsar-timing parameters used in the kinematic correction in Equation 2.10.

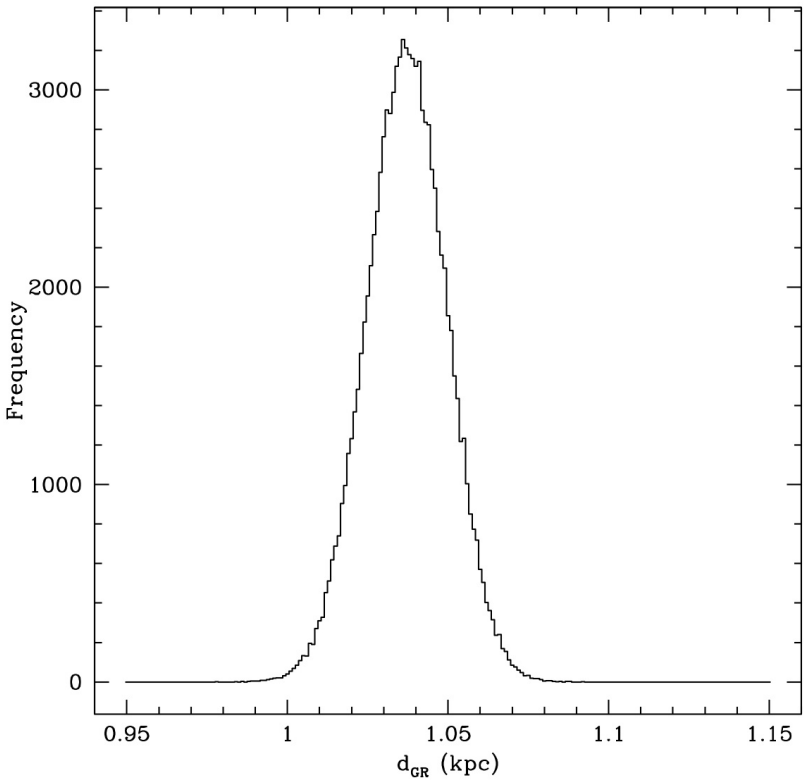

Figure 2.7: Distribution of theoretical distance to PSR B1534+12. We combined Equations 2.10 and 2.11, used the value of $(\dot{P}_b)^{\rm GR}$ obtained from the DDGR fit of our timing data, and solved for the distance required so that the measured value of $\dot{P}_b$ could be brought into agreement with general relativity. We estimated this distance and its uncertainty through Monte-Carlo sampling of input parameters shown in Figure 2.6.

the correct description of gravity. This means that $(\dot{P}_b)^{\rm true} = (\dot{P}_b)^{\rm GR}$, where the latter quantity is the value of $\dot{P}_b$ obtained by Equation 2.9b. We then combined Equations 2.10 and 2.11 to solve for a theoretical distance of PSR B1534+12, which we found to be

$$d_{\rm GR} = 1.037 \pm 0.012 \text{ kpc} \tag{2.12}$$

This value and its uncertainty were estimated by using a Monte Carlo sampling method: we randomly sampled a_z, R_0, v_0, and the "excess" $\dot{P}_b$ from normal distributions associated with each parameter's mean value and input uncertainty, as shown in Figure 2.6. We repeated this process 100,000 times, calculating a theoretical distance for each set of input parameters which lead to a normal-like distribution in $d_{\rm GR}$ shown in Figure 2.7. The distance obtained in this analysis agrees with the distance found by Stairs et al. (1998, 2002), but with greater precision and was computed without the small systematic mistakes that affected those measurements. Moreover, the relative uncertainty of this derived distance (~ 1.2 %) is slightly smaller than that of the derived distance estimate of PSR J0437-4715 made by Verbiest et al. (2008) and rivals high-precision distances from parallaxes measured with VLBA interferometry (Torres et al., 2007, 2009, 2012) and the Hawaii Infrared Parallax Program (Dupuy & Liu, 2012).

A downfall of the theoretical-distance method is that the orbital-decay measurement cannot be used as an unbiased test of gravitational theory until a significant, independent measurement of distance can be obtained. High-precision astrometry with the VLBA can provide possibly tighter constraints on the proper-motion contribution of the Galactic bias in $\dot{P}_b$ measured for PSR B1534+12, which will have sizable implications for the inclusion of another reliable test of relativity theory (Chatterjee et al., 2009).

2.4.3 Pulsar Jitter and Instrumental Limits on Timing Precision

Repeated observations and updated timing analyses of pulsars will lead to substantial improvements in their timing solutions. As demonstrated above, long-term timing observations and analyses of PSR B1534+12 provided a considerable refinement in relativistic parameters and tests of gravitational theory. However, unmodelable processes that affect pulse TOAs will serve as a limiting agent in high-precision timing. Figure 2.2 displays random pulsar jitter seen in PSR B1534+12, which we attributed to physical instabilities in neutron-star magnetosphere. We used this jitter as a means to justify our weighting of data with a minimum-error approach. This inherently

random process will persist even as more data is accumulated, meaning that the timing solution we present in this work will not be substantially improved in precision with further upgraded observing systems *for data taken at 430 MHz*. We are still limited at 1400 MHz by significantly smaller signal-to-noise, so updated observing machines can help mitigate this low-signal issue. Uncertainties in TOAs are still expected to decrease as more long-term data are accumulated. One method of approximating jitter is to average consecutive TOAs together; however, this will minimize coverage of the orbit and weaken constraints on the Keplerian and PK parameters.

Chapter 3

Profile Evolution and Relativistic Spin Precession in PSR B1534+12

A massive, isolated sphere with a well-defined vector of (spin) angular momentum will carry the same orientation relative to a distant observer. A similar "gyroscope" undergoing binary motion with another massive object will, in stark contrast, experience a systematic change in orientation due to the warped space-time in which this vector is being carried through (de Sitter, 1916). This effect, commonly referred to as "de-Sitter" or "geodetic" precession, will amount to a misalignment between the initial and final spin-angular momentum vector of the gyroscope relative to a distant observer after one full orbit. Another analogous effect, known as "Lense-Thirring" precession[14], will cause the orbit to precess given a *rotating* companion (Lense & Thirring, 1918). The resultant effect from both contributions is hereafter referred to as *relativistic spin precession*. Recent experiments carried out by the Gravity B probe measured geodetic and Lense-Thirring precession rates of several Earth-orbit gyroscopes that are in good agreement with the predictions of general relativity (Everitt et al., 2011).

In theory, binary pulsars serve as ideal candidates for studies on relativistic spin precession (Damour & Ruffini, 1974; Barker & O'Connell, 1975). These rapidly-rotating, compact objects can generally be approximated as point-like masses with large spin-angular momenta. Therefore, pulsars in binary orbits will undergo the same gravitational effects that gyroscopes experience as they orbit the Earth, but in a considerably stronger gravitational field. In practice, the precession of the pulsar's radio beam is detected as secular changes in the pulse profile over time; long-term evolution of pulse-profile components due to relativistic spin precession can then be seen as shifts in component amplitudes and/or locations across the pulse phase. The Hulse-Taylor pulsar provided the first evidence of relativistic spin precession

[14]this is also known as "frame dragging".

in a pulsar binary system (Weisberg et al., 1989). A subsequent study was able to derive the full geometry of the pulsar by assuming a cone-like radio beam structure, and associate each profile at a particular epoch as a slice of the beam model (Kramer, 1998). More recently, relativistic spin precession was inferred in the double-pulsar system (Lyne et al., 2004) by modeling the observed time-dependent flux decrement pattern of pulsar A at superior conjunction with the precessing pulsar B as a magnetospheric eclipsing event (Breton et al., 2008). The measured precession rate in the double-pulsar system agrees with general relativity to within $\sim 13\%$ of its predictions.

This chapter presents the current results[15] of an updated profile-evolution analysis using PSR B1534+12. Relativistic spin precession in PSR B1534+12 was first discovered by Arzoumanian (1995), although he was not able to measure orbital aberration with significance. A following analysis by Stairs et al. (2004) was able to derive a geodetic precession rate $\Omega_1^{\rm GR}$ for the pulsar that was in accordance with the prediction of general relativity (Barker & O'Connell, 1975),

$$\Omega_1^{\rm GR} = \frac{1}{2} T_\odot^{2/3} \left(\frac{P_b}{2\pi}\right)^{-5/3} \frac{m_2(4m_1 + 3m_2)}{(1-e^2)(m_1+m_2)^{4/3}} \tag{3.1}$$

where the quantities on the right hand side are the usual Keplerian and mass parameters as discussed in Chapter 2. The precession rate for PSR B1534+12 measured by Stairs et al. (2004) was $\Omega_1 = 0.44^{+4.6\circ}_{-0.2}$ yr^{-1} with 95% confidence. Using the high-precision timing measurements presented above, the expected precession rate for PSR B1534+12 is $\Omega_1^{\rm GR} = 0.51^\circ$ yr^{-1}. The study confirmed general relativity by examining a different physical effect, but did so with limited precision. Moreover, their study developed a general method for measuring the precession rate by simultaneously measuring the secular change in pulse-profile shape and relativistic aberration[16] of the profile across the orbit due to binary motion. This combination of effects allowed for direct measurement of the precession rate without the need for a beam-structure model, which is a key strength of the method. We therefore hoped that the inclusion of more pulse-profile data would better constrain the precession rate and even count as an additional test of relativity theory.

[15] This analysis is not complete and will be an ongoing study.

[16] To date, no other binary pulsar has exhibited the orbital aberration seen in PSR B1534+12.

Parameter	1998	1999	2000	2001	2003	2005	2008	Other
Observation type	camp.	camp.	camp.	camp.	camp.	camp.	camp.	ltt
Observation system	M-IV	M-IV	M-IV	M-IV	M-IV	M-IV, ASP	ASP	M-IV, ASP
Mean date (MJD)	51021	51317	51775	52080	52803	53549	54697	n/a
Orbital phase span	0.01-0.9	0.1-0.8	0.0-1.0	0.0-1.0	0.0-1.0	0.0-1.0	0.0-1.0	n/a
# of binned profiles used	7	4	10	9	9	8, 12	12	16, 20

Table 3.1: Logistics of pulse-profile data sets used in the profile-evolution analysis of PSR B1534+12. All data were collected using the Arecibo Observatory. The overall data set is comprised of six observational campaigns ("camp."; described below), with an overlap of observing machines during the 2005 campaign, along with high signal-to-noise long-term timing ("ltt") data.

3.1 Data Reduction and Observing Strategy

We used the same data set presented in Chapter 2 where 430-MHz data were available, which were the Mark IV and ASP data subsets. In the case of PSR B1534+12, profile evolution at 430 MHz can be more easily studied as the signal strength is substantially larger than its 1400-MHz counterpart (Stairs et al., 2000b). Raw data were processed and calibrated in the same manner as the data used above for pulsar timing. For this analysis, however, we were interested in the actual pulse profile itself, as opposed to the topocentric time at which the profile was observed. We therefore "rotated" every available profile to a common pulse phase for direct and consistent comparison. This was done by generating a set of polynomial coefficients at every epoch for Equation 1.1, using the "prediction" mode of TEMPO, based on the full timing solution derived in Chapter 2; these coefficients characterize the variation in observed pulse phase over the time span of our data set. Based on these sets of coefficients and the time-stamps of every profile, we shifted each profile to a pulse phase of zero.

Several observing strategies were used when collecting data over the years; these observing "types" can be broken into two categories: "long-term timing" and "campaign" observations. Long-term timing observations occurred on a relatively frequent ($\sim$ bi-monthly) basis, with an average observing time of forty minutes. These data were necessary for tracking DM variation over time, as demonstrated in Section 2.3.2 above, as well as providing an approximately continuous set of TOAs that is crucial for timing-precision purposes. We used individual long-terming time profiles with the highest signal-to-noise (S/N $\geq$ 250) in this precession study. In contrast, campaign observations were comprised of dense observing sessions that occurred every day for up to twelve days, and lasted several hours on each day. The purpose of these campaign sessions was to obtain the highest-S/N snapshot of the pulse profile at that particular epoch, as well as obtain pulse-profile data over the course of the pulsar's orbit. Full coverage of the orbit is important for studies of orbital aberration of the profile. The effects of precession and aberration on a pulse profile are generally anticipated to be measurable, albeit minute in scale. All profiles recorded during a campaign era were first binned by the orbital phase at which they were emitted, in order to build S/N as well as obtain a representative profile across different points of the binary orbit. Profiles within each bin were subsequently folded together to build S/N of the representative (average) profile. We divided the orbital phase into twelve bins for this analysis.

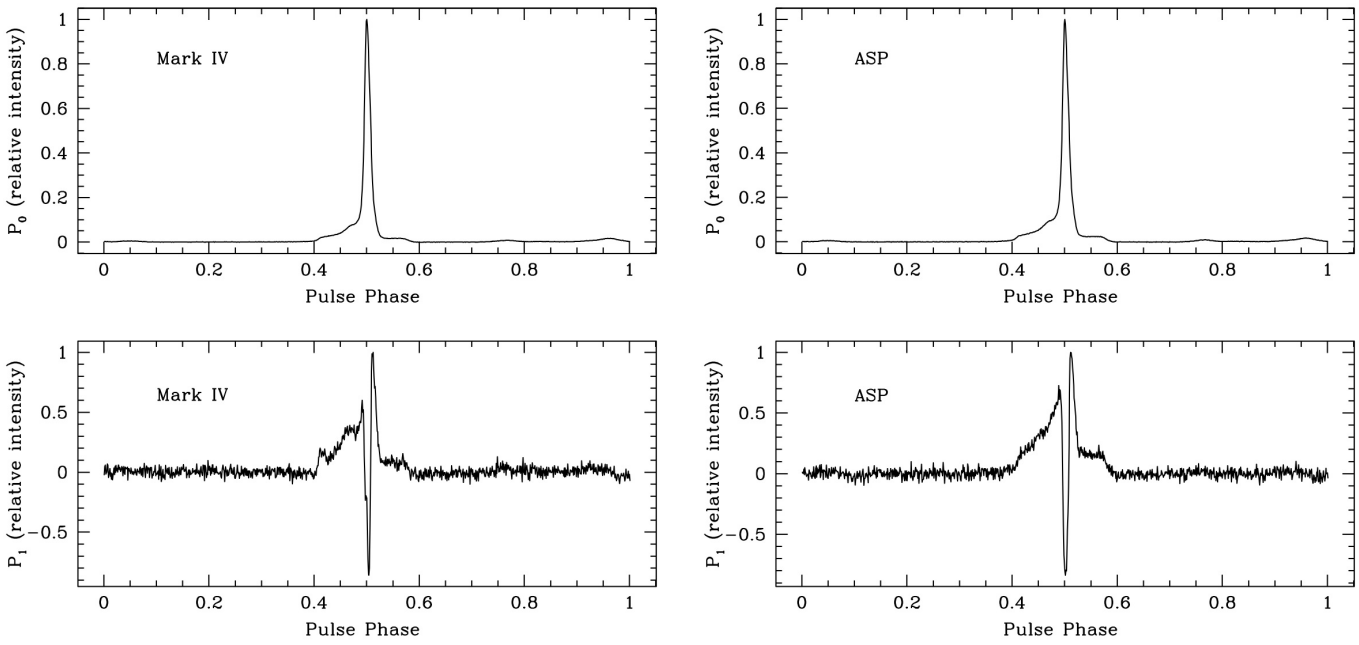

Figure 3.1: Principal-component analyses for the (complete) Mark IV and ASP profiles. The left pair of plots display the first (P_0) and second (P_1) principal components derived from 63 Mark IV profiles. The right pair shows the same two principal components, but derived from 44 ASP profiles. It is not immediately clear why the two P_1 components are different in shape, but possibilities for this difference can include: differences from 8-bit (ASP) vs. 4-bit (Mark IV) sampling; or physical/nonlinear changes in the pulse profile.

3.2 Methodology

Profile evolution due to pulsar precession is usually studied by assuming a model of the two-dimensional beam structure and associating the evolution with a secular change in beam orientation with respect to a distant observer (Kramer, 2002). However, Stairs et al. (2004) developed a general method for measuring a precession rate that is independent of the unknown beam model. We employed this procedure in this updated profile-evolution study.

The key concept is to measure several profile-evolution effects: the long-term (relativistic spin) precession of the pulsar; and the periodic aberration of the profile that is modulated from binary motion of the system. This is done by deriving a parameter that characterizes the overall shape of a given pulse profile; this quantity (F) is generally a function of time t, viewing angle ζ, and eccentric anomaly u of the orbit,

$$F(\zeta, t, u) = F(\zeta) + \frac{dF}{dt}(t - t_0) + \delta_A F(u) \tag{3.2}$$

For small changes in the viewing angle, $F(\zeta) \approx F(\zeta_0) + \zeta F'$, where $F' = dF/d\zeta$. Stairs et al. (2004) interpreted the F' quantity as the two-dimensional beam structure, a quantity that is initially unknown but can be assumed to stay constant across our data span. The time- and orbital-dependent effects are related to the precession rate and various geometrical quantities (Damour & Taylor, 1992), where Stairs et al. (2004) presented these equations as

$$\delta_A F = F' \frac{\beta_1}{\sin i}[-\cos\eta S(u) + \cos i \sin\eta C(u)], \tag{3.3a}$$

$$\frac{dF}{dt} = F' \Omega_1 \sin i \cos\eta \tag{3.3b}$$

Equation 3.3a represents the short-term contribution from orbital aberration: $\beta_1 = 2\pi x/(P_b\sqrt{1-e^2})$ is the characteristic velocity of the pulsar, and the Keplerian quantities (x, P_b, e) are measured from the pulsar-timing analysis presented above; $C(u) = \cos[\omega + A_e(u)] + e\cos\omega$ and $S(u) = \sin[\omega + A_e(u)] + e\sin\omega$ are functions of the periastron argument ω and the orbital argument u defined in Equations 1.4; i is the inclination of the orbit[17], which we measured through the Shapiro timing delay; and η is an angle subtended by the ascending node of the system and the projection

[17] We measured $\sin i = 0.978(3)$ from our timing analysis presented in Chapter 2. However, there is still an ambiguity of sign for $\cos i$.

of the pulsar spin axis. See Stairs et al. (2004) for a diagram of their derived spin, orbital geometry for the PSR B1534+12 system. Equation 3.3b represents the long-term change in profile shape due to relativistic spin precession. Both quantities are proportional to the unknown function F'. The beam-structure dependence can therefore be avoided by measuring and comparing both long- and short-term effects, allowing for a model-independent determination of Ω_1.

In accordance with the methodology developed by Stairs et al. (2004), we derived nominal "reference" (P_0) and "difference" (P_1) profiles for our sets of profile data using the principal-component analysis (PCA) method (Press et al., 1992). The two sets we performed the following precession study on are: the (complete) Mark IV data set; and the ASP data set. In each case, the two profiles PCA profiles characterized[18] the evolution across our data span and can be related to each of our observed pulse profiles P as a linear combination of time- and orbital-phase-dependent coefficients through the relation

$$P = c_0 P_0 + c_1 P_1 \tag{3.4}$$

We determined the (c_0, c_1) coefficients for every profile by applying this cross-correlation algorithm in the frequency domain. We then computed the quantity

$$F = \frac{c_1}{c_0} \tag{3.5}$$

which Stairs et al. (2004) defined as an indicator of profile shape that cancelled interstellar-scintillation effects on the pulse amplitude. We therefore used Equations 3.3, 3.4, 3.5 in order to solve for the shape F as a function of time, as well as the $C(u),\ S(u)$ quantities which characterize the aberration effect. We used an in-house computer program written by I. H. Stairs that simultaneously fits for the profile shape as a function of these quantities, based on the computed value of F and orbital phase of each profile in our data set.

[18] It should be acknowledged that an additional non-zero PCA component was obtained for the ASP data set, which could indicate higher-order evolution in the pulse profile at 430 MHz. However, we chose to only consider the first two principal components by using Equation 3.5 as the measure for profile shape.

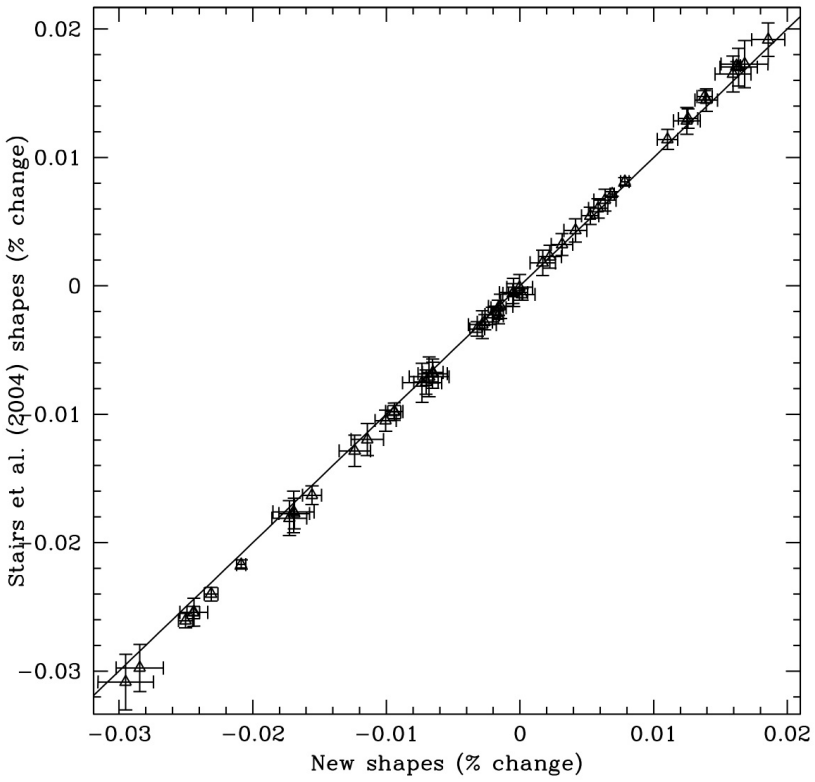

Figure 3.2: Comparison of profile shapes between the original Mark IV data set used by Stairs et al. (2004) and our version of 51 (out of 54) of their profiles. The line represents equality between shapes. The key difference between our data set and their original set is the timing solution that was used to rotate the profiles to a pulse phase of zero. We used the timing solution presented in this updated analysis, whereas they used the timing solution published by Stairs et al. (2002).

3.3 Current Results

As a test for this analysis, we ran the simultaneous linear-fitting program on our (rotated) versions of the same Mark IV profile data used by Stairs et al. (2004) in their study. Their analysis used a total of 54 profiles, but raw timing/profile data for three of these (long-term timing) profiles were not made available in time for this work, as they are stored on a hard disk at a different university. We therefore only use 51 of their profiles. The difference between their data and ours is that they rotated their profiles using the Stairs et al. (2002) timing solution, while we used the timing solution presented in Chapter 2 of this work. This check was carried out to confirm their results using an updated timing solution, prior to performing the full profile-evolution analysis that incorporated even more Mark IV data and the ASP profiles as well. Figure 3.2 shows that the shapes we calculated for our rotated set of profiles agree with the shapes of the same profiles used by Stairs et al. (2004), despite using a newer timing solution. Moreover, the simultaneous fit yielded a precession rate of $\Omega_1 = 0.52^{+8.9\circ}_{-0.3}$ yr^{-1} with 95% confidence, in agreement with their published results and with the value predicted by general relativity. The uncertainty in this measurement is estimated from a standard bootstrap method.

The next step was to to include pulse profiles collected *after* the analysis performed by Stairs et al. (2004) into this updated precession study. We first incorporated the remaining Mark IV data collected after their study – which is comprised of the 2005 Mark IV campaign and several long-term timing profiles – to our version of their 51 profiles. These profiles were also rotated to a pulse phase of zero, and selected for use based on their S/N value: eight of the twelve orbitally-binned 2005 campaign profiles were included in the analysis, as well as four long-term timing profiles. Therefore, we used a total of 63 data points for the complete Mark IV profile analysis. The shapes for each of these profiles were determined using the Mark IV PCA results shown in Figure 3.1. The results from this analysis are displayed in Figure 3.3, and once again confirm the result published by Stairs et al. (2004) with a measured precession rate of $\Omega_1 = 0.39^{+2.8\circ}_{-0.2}$ yr^{-1} with 95% confidence, and a derived angle $\eta = \pm 108 \pm 13^\circ$. The orbital aberration is also shown on the right-hand-side of Figure 3.3, where Mark IV profile shapes and best-fit aberration model are plotted against an "aberration angle",

$$\text{aberration angle} = \sin^{-1}(S(u) + \epsilon) \tag{3.6}$$

where ϵ is an arbitrary phase in order to shift the values of $S(u)$ to a range

for which the inverse-sine is well defined. We set $\epsilon = 0.26$ for all data sets, and chose to plot shapes against this angle in order to show the periodic change measured from the simultaneous fit due to orbital aberration of the profile.

However, computational problems arose when applying the same procedure to the ASP data set. PCA components for ASP profiles are shown in Figure 3.1, and the P_1 component has a noticeably different shape when compared to its Mark IV counterpart. It is not immediately clear if these differences reflect physical changes in the profile evolution itself, or the instrumental differences in bit sampling between the Mark IV and ASP machines mentioned in Chapter 2. Moreover, the results from the simultaneous-fit program using only the ASP profiles indicated that the range of values for $S(u)$ could not be shifted to a suitable range for calculating the aberration angle. The precession rate derived from this analysis is less consistent with the prediction from general relativity ($\Omega_1 = 0.14^{+0.2\circ}_{-0.1}$ yr^{-1} with 95% confidence), and the results are plotted in Figure 3.4. Four points were excluded from these plots *after* the simultaneous fit was applied to the ASP data, because the values of the quantity $(S(u) + \epsilon)$ lay outside of the range $-1 \leq S(u) + \epsilon \leq 1$. The best-fit model for long-term changes in F shows that precession is still occurring, but that the long-term change in profile shape is occurring at a different rate than indicated from the Mark IV analysis: the slope of Mark IV long-term shape evolution is $s = (2.14^{+0.1}_{-0.1}) \times 10^{-3}$ % day^{-1} with 95% confidence, while the analogous ASP slope is $s = (2.73^{+0.1}_{-0.2}) \times 10^{-3}$ % day^{-1} with 95% confidence. The best-fit aberration model has a slightly larger amplitude than the Mark IV aberration measurement, but has a comparable phase and yields $\eta = \pm 137 \pm 46^\circ$, which is consistent with the value derived from the Mark IV analysis. These issues in computation and discrepancies in PCA/fit results will be investigated further in order to obtain a better understanding of these differences and, hopefully, allow us to combine these two data sets for a global analysis of profile evolution over the fourteen-year data span of the Mark IV and ASP eras.

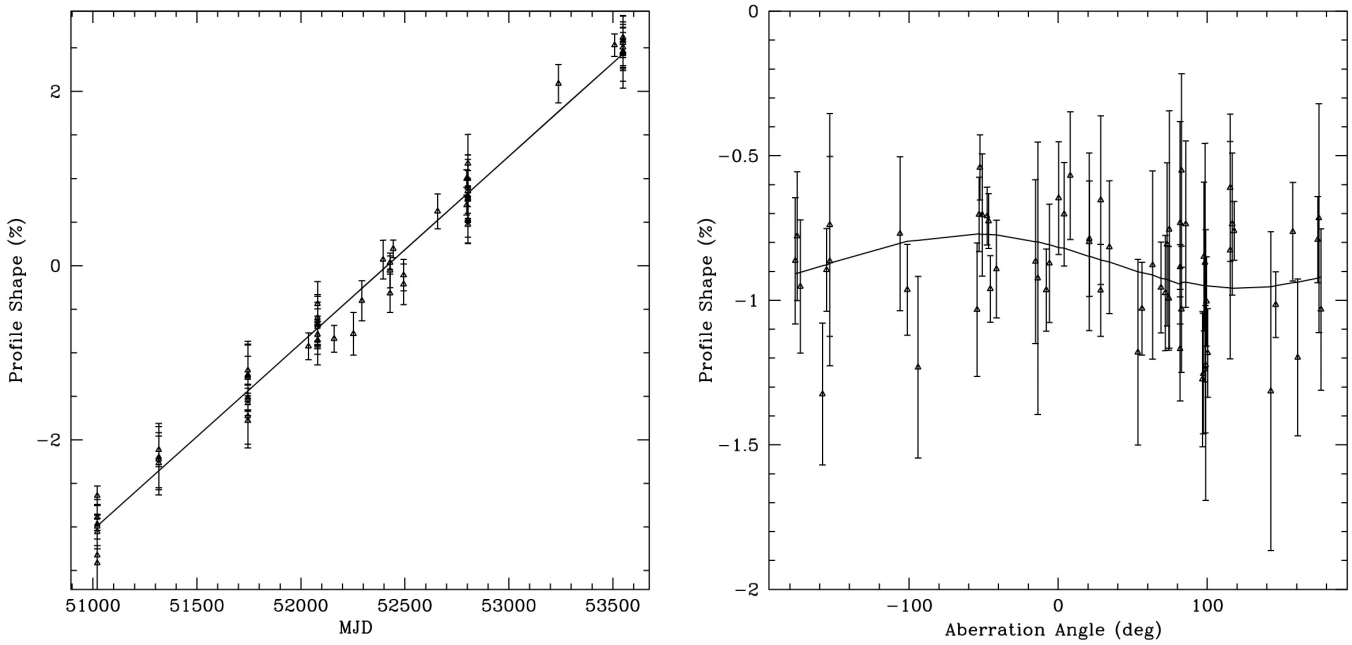

Figure 3.3: Measurement of relativistic spin precession in PSR B1534+12 using Mark IV 430-MHz data. The figure on the left plots the profile shape $F = c_1/c_0$ as a function of time; the figure on the right plots the profile shape F as a function of an aberration angle defined in the text. In both plots, the solid lines represent the best-fit models for long-term and aberrational precession, respectively. The measured precession rate from this analysis is $\Omega_1 = 0.39^{+2.8\circ}_{-0.2}\mathrm{yr}^{-1}$ with 95% confidence and agrees with the prediction of general relativity.

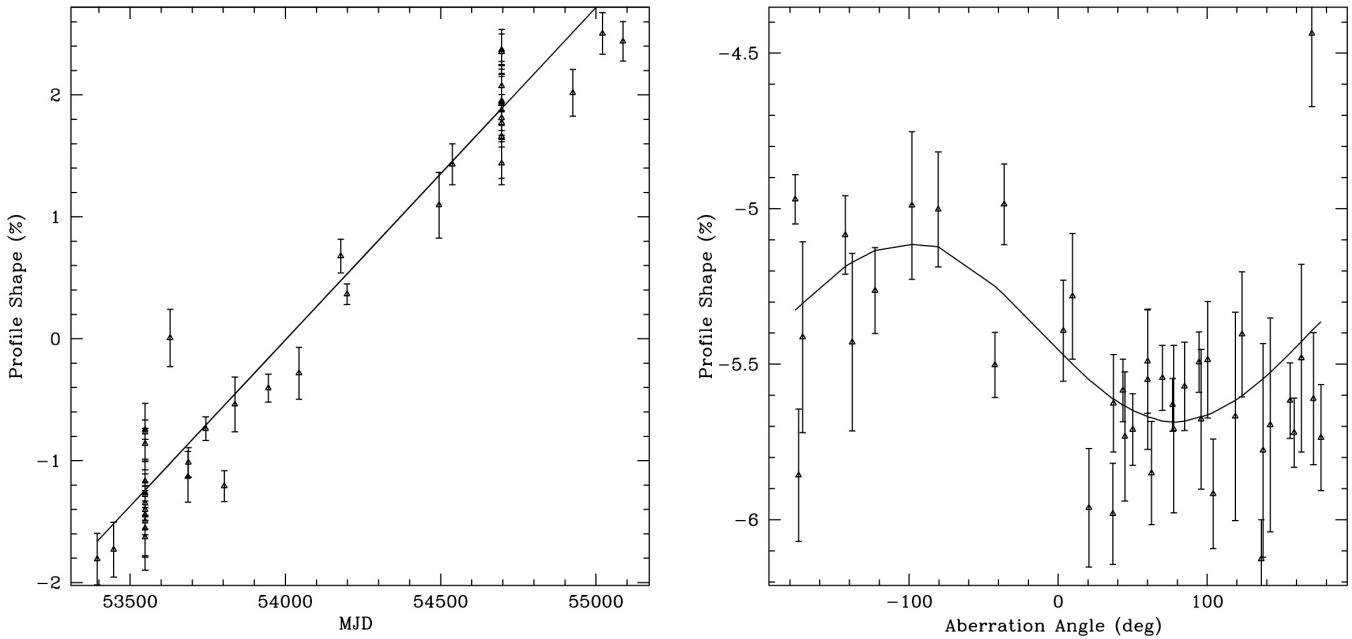

Figure 3.4: Measurement of relativistic spin precession in PSR B1534+12 using ASP 430-MHz data. This figure plots 40 ASP profile shapes $F = c_1/c_0$ as a function of time (left) and aberration angle (right); 44 profiles were used in the analysis, but 4 points were excluded due to an undefined aberration angle (see text). The solid lines in both plots represents the best-fit model for long-term precession and orbital aberration, respectively. The derived precession rate – $\Omega_1 = 0.14^{+0.2\circ}_{-0.1}\mathrm{yr}^{-1}$ with 95% confidence – is less consistent with the prediction of general relativity than the Mark IV analysis. See text for a discussion of these results.

Chapter 4

Summary, Conclusions, and the Future

We presented several analyses that probed relativistic gravity using the PSR B1534+12 binary system. An updated timing solution was derived by combining data sets collected over the past twenty-two years, and obtained with several generations of pulsar signal processors. This timing model accounted for every relevant astrophysical process that systematically affected every pulse TOA measured at the Arecibo Observatory in Puerto Rico. Such processes included: relative motion between the pulsar-binary and Solar systems; relativistic corrections associated with massive bodies within the Solar system; the (time-dependent) amount of electronic material along the line of sight to the pulsar; motion of the Earth about the Sun; binary motion between the pulsar and its companion; and relativistic parameters associated with the strong-field nature of the pulsar binary system. Five PK parameters were measured with improved significance, and four of these parameters were successfully used to confirm general relativity; our best test was the $\dot{\omega} - \gamma - s$ combination, which confirmed general relativity to within 0.35% of its predictions. The measurement of orbital decay in this system is biased due to relative motion of the two systems in the Galactic potential; the transformation between these references frames requires a reliable, independent measurement of distance, which we do not yet have. However, we were able to invert the problem and estimate a "theoretical" distance that would bring the observed value of orbital decay and the "excess" orbital decay due to the Galactic bias into agreement with the prediction from general relativity. This theoretical distance was estimated to be $d_{\rm GR} = 1.037 \pm 0.012$ kpc, in agreement with last timing study of PSR B1534+12 published by Stairs et al. (2002), and with significantly improved precision.

Other timing results were obtained that complemented the general-relativistic timing studies. We were able to estimate variation in the electron content of the Galaxy along the line of sight to PSR B1534+12 by binning pulsar DM across our data span and measuring time-derivatives within these bins. Furthermore, we examined pulse TOAs during a time-span where the

Mark IV and ASP observing machines overlapped in acquired data and obtained evidence for magnetospheric activity in PSR B1534+12. The implications from this pulse jitter are important, as it puts a type of floor on the lowest amount of timing precision allowed for this system with upgraded pulsar observing machines, at least at low observing frequencies where this pulsar is brightest. We argued that better instrumentation will not significantly decrease TOA uncertainties. However, future long-term timing of PSR B1534+12 will gradually produce fitted parameters with improved precision compared to the solution presented in this timing study.

We also performed tests on long-term changes in the pulse profile at 430 MHz, which previous studies have linked to geodetic precession. We carried out the same analysis performed by Stairs et al. (2004) on an extended set of Mark IV profiles, and were able to measure long-term and short-term changes in profile shape that we attributed to relativistic-spin precession and orbital aberration of the profile, respectively. We measured a precession rate of $\Omega_1 = 0.39^{+2.8\circ}_{-0.2}$ yr^{-1} with 95% confidence that is independent of pulse-beam structure. However, the ASP analysis produced somewhat conflicting results and yielded a precession rate of $\Omega_1 = 0.14^{+0.2\circ}_{-0.1}$yr^{-1} with 95% confidence, which is less consistent with the predictions of general relativity than the Mark IV test. The ASP profile still exhibited a long-term change in profile shape with a time-slope of $s = (2.73^{+0.1}_{-0.2}) \times 10^{-3}$ % day^{-1} with 95% confidence, and is significantly different than the corresponding Mark IV slope of $s = (2.14^{+0.1}_{-0.1}) \times 10^{-3}$ % day^{-1} also with 95% confidence. This may indicate an intrinsic change in profile shape that occurred towards the beginning of the ASP era, or instrumental differences between the Mark IV and ASP machines. The issues encountered with the ASP analysis require further scrutiny of the ASP data, the results obtained with these profiles, and possible solutions to these computational problems.

Future studies on this pulsar will primarily focus on the long-term evolution of timing parameters and pulse-profile shape, refining the current precession software, and developing different methods for extracting a precession rate of the pulsar. Stairs et al. (2004) measured changes in the polarization of the pulse signal from PSR B1534+12, and were able to infer the complete geometry of the pulsar-binary system by combining results from the profile-shape analysis mentioned above. This polarization study will be improved with the additional years' worth of data acquired since its publication in 2004. Moreover, long-term timing observations can continue tracking DM variation over time, as well as provide more insight into pulse jitter with the prospect of future observing systems. Subsequent astrometry of PSR B1534+12 with the VLBA or future SKA can provide high-precision

constraints on the distance to this objects, possibly allowing the inclusion of the orbital decay as another test of relativistic gravity.

Bibliography

Arzoumanian, Z. 1995, PhD thesis, Princeton University

Backer, D. C. & Hellings, R. W. 1986, Ann. Rev. Astr. Ap., 24, 537

Barker, B. M. & O'Connell, R. F. 1975, ApJ, 199, L25

Bell, J. F. & Bailes, M. 1996, ApJ, 456, L33

Breton, R. P., Kaspi, V. M., Kramer, M., McLaughlin, M. A., Lyutikov, M., Ransom, S. R., Stairs, I. H., Ferdman, R. D., & Camilo, F. 2008, Science

Chatterjee, S., Brisken, W. F., Vlemmings, W. H. T., Goss, W. M., Lazio, T. J. W., Cordes, J. M., Thorsett, S. E., Fomalont, E. B., Lyne, A. G., & Kramer, M. 2009, ApJ, 698, 250

Cordes, J. M. & Lazio, T. J. W. 2002, preprint (arXiv:astro-ph/0207156)

Cordes, J. M. & Shannon, R. M. 2012, ApJ, 750, 89

Damour, T. & Deruelle, N. 1985, Ann. Inst. H. Poincaré (Physique Théorique), 43, 107

—. 1986, Ann. Inst. H. Poincaré (Physique Théorique), 44, 263

Damour, T. & Ruffini, R. 1974, Academie des Sciences Paris Comptes Rendus Ser. Scie. Math., 279, 971

Damour, T. & Taylor, J. H. 1992, Phys. Rev. D, 45, 1840

de Sitter, W. 1916, MNRAS, 77, 155

Demorest, P. B. 2007, PhD thesis, University of California, Berkeley

Demorest, P. B., Pennucci, T., Ransom, S. M., Roberts, M. S. E., & Hessels, J. W. T. 2010, Nature, 467, 1081

Dupuy, T. J. & Liu, M. C. 2012, ApJ, 201, 19

Everitt, C. W. F., Debra, D. B., Parkinson, B. W., Turneaure, J. P., Conklin, J. W., Heifetz, M. I., Keiser, G. M., Silbergleit, A. S., Holmes, T., Kolodziejczak, J., Al-Meshari, M., Mester, J. C., Muhlfelder, B., Solomonik, V. G., Stahl, K., Worden, Jr., P. W., Bencze, W., Buchman, S., Clarke, B., Al-Jadaan, A., Al-Jibreen, H., Li, J., Lipa, J. A., Lockhart, J. M., Al-Suwaidan, B., Taber, M., & Wang, S. 2011, Phys. Rev., 106, 221101

Ferdman, R. D. 2008, PhD thesis, University of British Columbia

Goldreich, P. & Julian, W. H. 1969, ApJ, 157, 869

Hankins, T. H. & Rickett, B. J. 1975, in Methods in Computational Physics Volume 14 — Radio Astronomy (New York: Academic Press), 55

Hewish, A., Bell, S. J., Pilkington, J. D. H., Scott, P. F., & Collins, R. A. 1968, Nature, 217, 709

Hulse, R. A. & Taylor, J. H. 1975, ApJ, 195, L51

Kaspi, V. M., Taylor, J. H., & Ryba, M. 1994, ApJ, 428, 713

Konopliv, A. S., Yoder, C. F., Standish, E. M., Yuan, D. N., & Sjogren, W. L. 2006, Icarus, 182, 23

Kramer, M. 1998, ApJ, 509, 856

Kramer, M. 2002, in IX Marcel Grossmann Meeting, ed. R. J. V.G. Gurzadyan & R. Ruffini (World Scientific)

Kramer, M., Stairs, I. H., Manchester, R. N., McLaughlin, M. A., Lyne, A. G., Ferdman, R. D., Burgay, M., Lorimer, D. R., Possenti, A., D'Amico, N., Sarkissian, J. M., Hobbs, G. B., Reynolds, J. E., Freire, P. C. C., & Camilo, F. 2006, Science, 314, 97

Kuijken, K. & Gilmore, G. 1989, MNRAS, 239, 571

Lattimer, J. M. & Prakash, M. 2004, Science, 304, 536

Lense, J. & Thirring, H. 1918, Phys Z, 19, 156

Lorimer, D. R. 2001, Living Reviews in Relativity, http://www.livingreviews.org/Articles/Volume4/2001-5lorimer

—. 2005, Living Reviews in Relativity, http://relativity.livingreviews.org/Articles/lrr-2005-7/

Lorimer, D. R. & Kramer, M. 2005, Handbook of Pulsar Astronomy (Cambridge University Press)

Lyne, A. G., Burgay, M., Kramer, M., Possenti, A., Manchester, R. N., Camilo, F., McLaughlin, M. A., Lorimer, D. R., D'Amico, N., Joshi, B. C., Reynolds, J., & Freire, P. C. C. 2004, Science, 303, 1153

Lyne, A. G., Manchester, R. N., & Taylor, J. H. 1985, MNRAS, 213, 613

Lyne, A. G. & Smith, F. G. 2004, Pulsar Astronomy, 3rd ed. (Cambridge: Cambridge University Press)

Manchester, R. N. & Taylor, J. H. 1977, Pulsars (San Francisco: Freeman)

Nice, D. J. & Taylor, J. H. 1995, ApJ, 441, 429

Press, W. H., Teukolsky, S. A., Vetterling, W. T., & Flannery, B. P. 1992, Numerical Recipes: The Art of Scientific Computing, 2^{nd} edition (Cambridge: Cambridge University Press)

Ramachandran, R., Demorest, P., Backer, D. C., Cognard, I., & Lommen, A. 2006, ApJ, 645, 303

Shapiro, I. I. 1964, Phys. Rev. Lett., 13, 789

Shklovskii, I. S. 1970, Sov. Astron., 13, 562

Stairs, I. H. 2003, Living Reviews in Relativity, 5, uRL (Cited on 2008/02/16): http://relativity.livingreviews.org/Articles/lrr-2003-5

Stairs, I. H. 2004, Science, 304, 547

Stairs, I. H. 2005, in Binary Radio Pulsars, ed. F. Rasio & I. H. Stairs (San Francisco: Astronomical Society of the Pacific), 3

Stairs, I. H., Arzoumanian, Z., Camilo, F., Lyne, A. G., Nice, D. J., Taylor, J. H., Thorsett, S. E., & Wolszczan, A. 1998, ApJ, 505, 352

Stairs, I. H., Splaver, E. M., Thorsett, S. E., Nice, D. J., & Taylor, J. H. 2000a, MNRAS, 314, 459, (astro-ph/9912272)

Stairs, I. H., Thorsett, S. E., & Arzoumanian, Z. 2004, Phys. Rev. Lett., 93, 141101

Stairs, I. H., Thorsett, S. E., Taylor, J. H., & Arzoumanian, Z. 2000b, in Pulsar Astronomy - 2000 and Beyond, IAU Colloquium 177, ed. M. Kramer, N. Wex, & R. Wielebinski (San Francisco: Astronomical Society of the Pacific), 121

Stairs, I. H., Thorsett, S. E., Taylor, J. H., & Wolszczan, A. 2002, ApJ, 581, 501

Standish, E. M. 1990, A&A, 233, 252

Stinebring, D. R., Kaspi, V. M., Nice, D. J., Ryba, M. F., Taylor, J. H., Thorsett, S. E., & Hankins, T. H. 1992, Rev. Sci. Instrum., 63, 3551

Taylor, J. H. 1992, Philos. Trans. Roy. Soc. London A, 341, 117

Taylor, J. H. & Cordes, J. M. 1993, ApJ, 411, 674

Taylor, J. H. & Weisberg, J. M. 1982, ApJ, 253, 908

—. 1989, ApJ, 345, 434

Taylor, J. H., Wolszczan, A., Damour, T., & Weisberg, J. M. 1992, Nature, 355, 132

Torres, R. M., Loinard, L., Mioduszewski, A. J., Boden, A. F., Franco-Hernández, R., Vlemmings, W. H. T., & Rodríguez, L. F. 2012, ApJ, 747, 18

Torres, R. M., Loinard, L., Mioduszewski, A. J., & Rodríguez, L. F. 2007, ApJ, 671, 1813

—. 2009, ApJ, 698, 242

Verbiest, J. P. W., Bailes, M., van Straten, W., Hobbs, G. B., Edwards, R. T., Manchester, R. N., Bhat, N. D. R., Sarkissian, J. M., Jacoby, B. A., & Kulkarni, S. R. 2008, ApJ, 679, 675

Weisberg, J. M., Nice, D. J., & Taylor, J. H. 2010, ApJ, 722, 1030

Weisberg, J. M., Romani, R. W., & Taylor, J. H. 1989, ApJ, 347, 1030

Wolszczan, A. 1991, Nature, 350, 688

Wolszczan, A. & Frail, D. A. 1992, Nature, 355, 145

You, X. P., Hobbs, G., Coles, W. A., Manchester, R. N., Edwards, R., Bailes, M., Sarkissian, J., Verbiest, J. P. W., van Straten, W., Hotan, A., Ord, S., Jenet, F., Bhat, N. D. R., & Teoh, A. 2007, MNRAS, 378, 493